

EELG1002: A Record-Breaking [OIII]+H β EW \sim 3700Å Galaxy at $z \sim 0.8$ – Analog of Early Galaxies?

ALI AHMAD KHOSTOVAN ^{1,2}, JEYHAN S. KARTALTEPE ¹, MALTE BRINCH ^{3,4}, CAITLIN CASEY ^{5,3}, ANDREAS FAISST ⁶,
SANTOSH HARISH ¹, GHASSEM GOZALIASL ^{7,8}, MASATO ONODERA ^{9,10} AND KIYOTO YABE ⁹

¹Laboratory for Multiwavelength Astrophysics, School of Physics and Astronomy, Rochester Institute of Technology, 84 Lomb Memorial Drive, Rochester, NY 14623, USA

²Department of Physics and Astronomy, University of Kentucky, 505 Rose Street, Lexington, KY 40506, USA

³Cosmic Dawn Center (DAWN), Denmark

⁴DTU-Space, National Space Institute, Technical University of Denmark, Elektrovej 327, DK-2800 Kgs. Lyngby, Denmark

⁵The University of Texas at Austin, 2515 Speedway Blvd Stop C1400, Austin, TX 78712, USA

⁶Caltech/IPAC, 1200 E. California Blvd., Pasadena, CA, 91125 USA

⁷Department of Computer Science, Aalto University, PO Box 15400 Espoo, 00 076 Finland

⁸Department of Physics, University of Helsinki, PO Box 64 00014 Helsinki, Finland

⁹Subaru Telescope, National Astronomical Observatory of Japan, National Institutes of Natural Sciences (NINS), 650 North A'ohoku Place, Hilo, HI 96720, USA

¹⁰Department of Astronomical Science, The Graduate University for Advanced Studies, SOKENDAI, 2-21-1 Osawa, Mitaka, Tokyo 181-8588, Japan

ABSTRACT

Extreme emission line galaxies (EELGs) are powerful low- z analogs of high- z galaxies that can provide us valuable insights of early Universe conditions. We present a detailed analysis of EELG1002: a $z = 0.8275$ EELG identified within archival Gemini/GMOS spectroscopy as part of the on-going COSMOS Spectroscopic Archive. We find EELG1002 is a low-mass ($\sim 10^8 M_\odot$), compact (~ 530 pc), bursty star-forming galaxy with a $\sim 15 - 35$ Myr mass doubling timescale. EELG1002 has record-breaking rest-frame [OIII]+H β EW $\sim 3100 - 3700\text{\AA}$; $\sim 32 - 36\times$ higher than typical $z \sim 0.8$ [OIII] emitters with similar stellar mass and higher than typical $z > 5$ galaxies. We find no clear evidence of an AGN suggesting the emission lines are star formation driven. EELG1002 is chemically unevolved (direct T_e ; $12 + \log_{10}(\text{O}/\text{H}) \sim 7.52$ consistent with $z > 5$ galaxies at fixed stellar mass) and may be undergoing a first intense, bursty star formation phase analogous to conditions expected of galaxies in the early Universe. We find evidence for a highly energetic ISM ([OIII]/[OII] ~ 9) and hard ionizing radiation field (elevated [NeIII]/[OII] at fixed [OIII]/[OII]). Coupled with its compact, metal-poor, and actively star-forming nature, EELG1002 is found to efficiently produce ionizing photons ($\xi_{\text{ion}} \sim 10^{25.74} \text{ erg}^{-1} \text{ Hz}$) and may have $\sim 10 - 20\%$ LyC escape suggesting such sources may be important analogs of galaxies responsible for reionization. We find dynamical mass of $\sim 10^9 M_\odot$ suggesting copious amounts of gas to support intense star formation as also suggested by identified Illustris-TNG analogs. EELG1002 may be an ideal low- z laboratory of galaxies in the early Universe and demonstrates how archival datasets can support high- z science and next-generation surveys planned with *Euclid* and *Roman*.

Keywords: Galaxy Evolution (594), High-redshift Galaxies (734), Interstellar medium (847), Starburst Galaxies (1570), Star Formation (1569)

1. INTRODUCTION

Understanding how star-formation occurred in the early Universe is crucial in our understanding of how galaxy formation and cosmic Reionization occurred. Prior to *JWST*, it was very difficult to observe galaxies at $z > 6$ and was pri-

marily limited to samples selected as Lyman Break Galaxies (LBGs; e.g., Bouwens et al. 2011; McLure et al. 2013; Oesch et al. 2014; McLeod et al. 2016; Ishigaki et al. 2018; Finkelstein et al. 2022), Ly α emitters (e.g., Rhoads et al. 2000; Malhotra & Rhoads 2004; Dawson et al. 2007; Matthee et al. 2014; Santos et al. 2016; Konno et al. 2018; Sobral et al. 2018; Taylor et al. 2020; Goto et al. 2021; Wold et al. 2022; Torralba-Torregrosa et al. 2024), and galaxies selected based on nebular excess within the *Spitzer*/IRAC bands (e.g., Shim et al. 2011; Smit et al. 2015; Faisst et al. 2016; Mármol-

Queralto et al. 2016; Rasappu et al. 2016; De Barros et al. 2019; Lam et al. 2019; Endsley et al. 2021b). However, in only the first few years of *JWST* we are detecting numerous $z > 6$ galaxies that were missed in past selection techniques and also galaxies with redshifts in the double digits. *JWST* has pushed our observable window further towards the era that we expect harbors the first generation of galaxies. However, local analogs of high- z galaxies can still provide us with valuable insight on the conditions of galaxies in the early Universe that are still limiting with even *JWST*.

Extreme Emission Line Galaxies (EELGs) are a unique subset of galaxies known for having strong nebular emission line features with high equivalent widths (EWs; ratio of line flux to continuum flux density) at a level that can dominate some of the widest broadband filters. Other names associated with EELGs include ‘Green Peas’ ($z \sim 0.2 - 0.3$; Cardamone et al. 2009; Izotov et al. 2011) and ‘Blueberries’ ($z < 0.05$; Yang et al. 2017b) given their strong nebular contribution in the SDSS r and g bands, respectively. EELGs are known to be low-mass systems (e.g., Maseda et al. 2014; Amorín et al. 2015; Forrest et al. 2017; Yang et al. 2017b) with compact sizes (e.g., van der Wel et al. 2011; Amorín et al. 2015; Forrest et al. 2017; Yang et al. 2017a; Kim et al. 2021) typical of galaxies at $z > 3$ (e.g., Yang et al. 2022b; Ormerod et al. 2024), and with elevated star-formation rates and mass doubling timescales of < 100 Myr (e.g., Atek et al. 2011; Maseda et al. 2013; Atek et al. 2014; Amorín et al. 2015). Past studies reveal that EELGs are low in gas-phase metallicities (e.g., Amorín et al. 2014a,b; Jiang et al. 2019) with energetic ISM conditions (elevated [OIII]/[OII] ratios; e.g., Izotov et al. 2018; Paalvast et al. 2018; Izotov et al. 2021a). EELGs also exhibit LyC escape with high ionizing photon production efficiencies (ξ_{ion}) owing to their compact, star-forming nature and high [OIII]/[OII] ratios (e.g., Schaerer et al. 2016; Tang et al. 2019; Emami et al. 2020; Atek et al. 2022). This makes EELGs powerful analogs of sources that contribute towards cosmic reionization in the high- z Universe where measurements of LyC escape are extremely difficult given the IGM transmission at $z > 3$ (e.g., Madau 1995; Inoue et al. 2014). It also allows for detailed analysis on the conditions and mechanisms associated with LyC escape that are expected to occur during the Epoch of Reionization.

Strong nebular features (e.g., [OIII], $H\beta$, $H\alpha$) confirm recent and intense star-formation activity. Tang et al. (2022) used non-parametric star formation history modeling and found that EELGs not only go through a recent, intense burst of star-formation but may have also gone through past bursts highlighting episodic SFHs. Cohn et al. (2018) suggests that high EW systems at high- z represent galaxies undergoing a first bursty phase of star-formation activity given that stellar mass buildup has not fully taken effect (fainter continuum flux densities) resulting in higher [OIII]+ $H\beta$ EW. After each

subsequent burst, the stellar continuum increases in brightness resulting in lower EWs. Hydrodynamical simulations and simple analytical models also suggest that star formation activity in high- z galaxies is burst-dominated (e.g.; Sparre et al. 2017; Faucher-Giguère 2018). Given that high EWs are ubiquitous of high- z galaxy populations (e.g., Smit et al. 2014; Khostovan et al. 2024), identifying high EW EELGs in the low- z Universe provides an interesting window in studying the star formation processes expected to occur in the high- z Universe. Coupled with past confirmations of LyC escape and elevated ξ_{ion} , low- z EELGs are a window to explore how star formation processes and ionizing photon production of low-mass, star-forming galaxies can contribute towards the cosmic ionizing photon budget needed to facilitate cosmic reionization.

In this paper, we present a detailed analysis of EELG1002 ($\alpha = 10 : 00 : 32.304$, $\delta = +2 : 51 : 11.351$): a record-breaking $z \sim 0.8$ EELG that was serendipitously identified within archival Gemini/GMOS spectroscopy as part of ongoing work in developing the COSMOS Spectroscopic Archive. This source has properties that are strongly consistent with some of the most extreme star-forming galaxies currently being observed with *JWST* at $z > 6$ and provides an ideal low- z laboratory to investigate the star-formation, ISM, and ionizing properties of galaxies that exist in the high- z Universe. In this work, we investigate EELG1002 in great detail using a combination of GMOS spectra, detailed spectrophotometric SED fitting, morphology measurements, and analogs within hydrodynamical simulations to investigate the nature of this source within the context of star-formation processes, ISM conditions, and potential as an important contributor of ionizing photons. The main objective of this paper is to first highlight the importance of such a high EW EELG and motivate for further search of EELG1002-like systems to develop larger statistical samples for analysis. Second, we aim to demonstrate the power of using archival data in finding such hidden gems that can enable new science and support future science objectives.

The structure of this paper is as follows: §2 outlines the Gemini/GMOS observations of EELG1002 along with the ancillary data from COSMOS2020 (Weaver et al. 2022) and additional *HST*/WFC3 F140W imaging (Silverman et al. 2018; Ding et al. 2020). §3 presents our approach in reducing the spectroscopic data, determining the spectroscopic redshift, emission line profile fitting, and measuring the velocity dispersion, ISM properties, EWs, ionizing photon production efficiency, sizes, and SED fitting procedure. We present all our results in §4 using all available spectroscopic and photometric evidence to characterize the nature of EELG1002 and how it is analogous to $z > 6$ galaxies currently being observed with *JWST*. We present further discussion in §5 in regards to the star-formation history showing how it is supported by

154 elevated gas masses by using both measurements of dynamical
 155 masses and EELG1002-like sources within Illustris-TNG.
 156 We also discuss the descendants of sources like EELG1002,
 157 the feasibility of LyC escape, and how EELG1002 may be an
 158 ideal case of studying reionization-era galaxies in the low- z
 159 Universe. §6 outlines the main conclusions of this paper.

160 Throughout this paper, we assume a Λ CDM cosmology
 161 with $H_0 = 70 \text{ km s}^{-1} \text{ Mpc}^{-1}$, $\Omega_m = 0.3$ and $\Omega_\Lambda = 0.7$. All
 162 magnitudes, unless otherwise stated, follow the AB magni-
 163 tude system.

164 2. DATA

165 The COSMOS Spectroscopic Archive (Khostovan et al.,
 166 in prep) is a great effort of gathering and processing all
 167 ground-based spectroscopic observations done over the past
 168 two decades with the COSMOS legacy field (Scoville et al.
 169 2007). As part of our search, we came across EELG1002
 170 within the Gemini Science Archive which was part of a Fast
 171 Turnaround program, GS-2017A-FT-9 (PI: Kiyoto Yabe).
 172 The main focus of the program was to target emission line
 173 galaxies at $z > 0.3$ that were identified by strong nebular ex-
 174 cess within the Subaru/HSC broadband filters indicative of
 175 high EW emission lines. These sources are expected to have
 176 strong [OIII] EW of $> 2000\text{\AA}$ and are metal-poor with the
 177 possibility of [OIII]4363Å detection.

178 2.1. GMOS Spectroscopy

179 GS-2017A-FT-9 consisted of three masks with only one
 180 in COSMOS which is the focus of this paper. Observations
 181 were taken on 23 April 2017 with Gemini-South using the
 182 Gemini Multiobject Spectrograph (GMOS) and its Hama-
 183 matsu Detector, R150 grating, and GG455 blocking filter.
 184 This allows for spectral coverage from 4600Å to 10000Å.
 185 Seeing conditions were reported as 0.9'' throughout the ob-
 186 serving time and humidity levels were somewhat elevated at
 187 $\sim 40\%$. A total of 3 individual exposures each having a dif-
 188 ferent dispersion angle were pointed at GS2017AFT009-02
 189 (mask design file) with the central wavelengths of each ex-
 190 posure being 8070Å, 8200Å, and 8330Å, respectively, which
 191 when 2D coadded would take into account the GMOS detec-
 192 tor chip gaps allowing for continuous spectral coverage in the
 193 final 1D and 2D spectra. Each science exposure was 1200
 194 seconds resulting in an on-source integration time of 3600
 195 seconds. The slit widths were set to 0.5'' for the science tar-
 196 gets and box slits of 2'' sizes were used for alignment stars.
 197 A single 5-sec twilight flat and 1-sec dome flat was taken
 198 per dispersion angle totaling 3 twilight flats and 3 dome flats.
 199 A single 20-sec CuAr arc lamp exposure was also taken for
 200 wavelength calibrations per each dispersion angle. The bias
 201 frames were taken on 29 April 2017 (the last night of the pro-
 202 gram) and consisted of 5 frames each 1 second in exposure
 203 time.

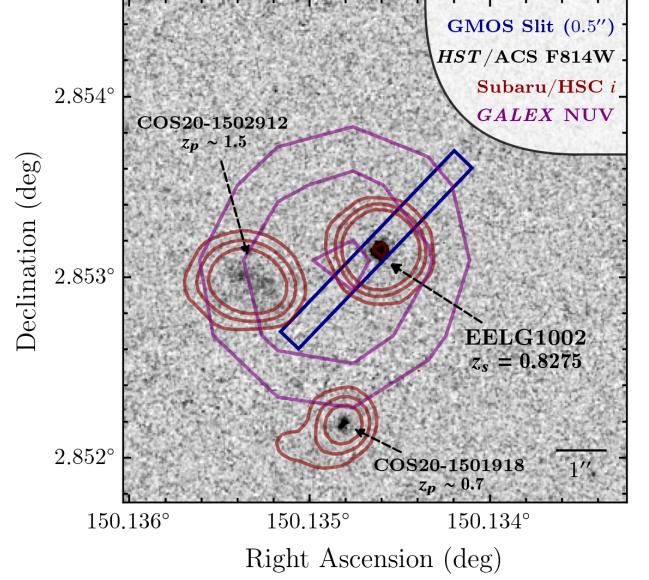


Figure 1. GMOS slit position (blue) for EELG1002 with a $10'' \times 10''$ HST/ACS F814W cutout ($0.03'' \text{ pix}^{-1}$ resolution; background). Subaru/HSC i detection is shown in red contours highlighting the lower resolution of ground-based observations where we find $\sim 50\%$ of EELG1002's total flux is observed along the $0.5''$ GMOS slit. EELG1002 has GALEX/NUV (purple contours) and FUV detections which would suggest strong Ly α emission and possible LyC escape, respectively; however, GALEX spatial resolution is quite poor. The proximity of two nearby sources along line-of-sight, shown with their COSMOS2020/Classic IDs and best-fit photometric redshifts, suggests the GALEX detections suffer blending issues. We therefore ignore GALEX, as well as *Spitzer*, photometry in this analysis due to blending issues.

204 The standard star LTT7379 (G0 star) that we used for flux
 205 calibration purposes was observed on 29 April 2017 with the
 206 same configuration and central wavelength of 8200Å. Seeing
 207 was reported as 1.08'' with humidity levels of 14%. Observa-
 208 tions of the standard star were performed using a 0.5'' wide
 209 long-slit for an on-source integration time of 10 seconds. A
 210 single 1-sec CuAr arc lamp and dome flat were observed with
 211 the same configuration and slit widths.

212 2.2. COSMOS2020 Classic

213 We cross-match EELG1002 with the COS-
 214 MOS2020/Classic catalog (Weaver et al. 2022) which has
 215 high-quality, multi-wavelength photometry enabling us to
 216 investigate its spectral energy distribution (SED). A total
 217 of 38 photometric bands are included from space-based
 218 missions (GALEX, HST, Spitzer) and ground-based ob-
 219 servatories (CFHT/MegaCam, Subaru/SuprimeCam, Sub-
 220 aru/HyperSuprimeCam, Paranal/VISTA). The available pho-
 221 tometry used in this work is highlighted in Table 1. We
 222 choose to ignore GALEX and Spitzer photometry due to
 223 blending issues from 2 nearby sources as shown in Figure

1 but note that future *HST*/COS and *JWST* imaging would help spatially resolve and constrain the rest-frame UV and infrared properties of EELG1002. In total, we used 32 photometric bands with 29 drawn from COSMOS2020/Classic and a single *HST*/WFC3 F140W detection drawn from ancillary imaging as described below (§2.3). The *CFHT*/WIRCam *H* and *K_s* photometry was drawn from COSMOS2015 (Laigle et al. 2016) due to the lack of UltraVISTA *YJHK_s* coverage of EELG1002.

2.3. *HST*/WFC3 F140W imaging

Ancillary *HST*/WFC3 F140W imaging of EELG1002 was found on the MAST portal. The associated program, PID #15115 (PI: John Silverman; Silverman et al. 2018; Ding et al. 2020), targeted a sample of $z \sim 1.5$ broad-line AGN to study supermassive black hole properties and how it relates to galaxy mass. One of their main targets, LID360, happened to be oriented such that EELG1002 fell within the *HST* FoV with a total exposure time of ~ 2400 seconds. Post-processing and photometry measurements were made as part of the Hubble Advance Program (HAP) Single Visit Mosaics (SVM) program. EELG1002 was found to have a F140W magnitude of 23.89 ± 0.08 mag within a $2''$ aperture (large enough to encompass the full source; see Figure 1).

3. METHODOLOGY

3.1. Data Reduction

We reduce all raw spectroscopic data using *PyPeit* (Prochaska et al. 2020a; v1.10dev – `gemini_gmos_mask_ingestion` branch¹), a Python semi-automated data reduction pipeline that supports many ground- and space-based facilities. The pipeline starts by reading the setup files that list the location of the science/standard & associated calibration frames. These setup files are made available via the linked GitHub repository² for anyone to reproduce the final spectra shown in this work. The first main script of the pipeline automatically does bias & overscan subtraction, slit edge detections, flat fielding, removal of cosmic rays, wavelength calibrations, tilt corrections, sky subtraction, flexure corrections, and a first pass on object extraction using the Horne (1986) optimal extraction algorithm.

The second step in the pipeline is to 2D coadd all 3 reduced science frames of varying central wavelengths (accounts for GMOS chip gaps in final 2D coadded spectra). To account for potential drift during observations, we define the offsets

Table 1. Multiwavelength photometry of EELG1002 used in our SED fitting. All data are drawn from the COSMOS2020 Classic (Weaver et al. 2022) except for *CFHT*/WIRCam (COSMOS2015; Laigle et al. 2016) and *HST*/WFC3 F140W (§2.3). EELG1002 has *GALEX* and *Spitzer* detections but we do not include them in our SED fitting due to blending issues with 2 nearby sources.

Band	λ_c (Å)	FWHM (Å)	mag _{AUTO} (AB mag)
CFHT/MegaCam			
<i>u</i>	3709	518	23.84 ± 0.01
<i>u</i> *	3858	598	23.93 ± 0.01
Subaru/HyperSuprimeCam			
<i>g</i>	4847	1383	23.84 ± 0.01
<i>r</i>	6219	1547	23.82 ± 0.01
<i>i</i>	7699	1471	23.82 ± 0.01
<i>z</i>	8894	766	22.12 ± 0.01
<i>y</i>	9761	786	24.20 ± 0.04
Subaru/SuprimeCam			
<i>B</i>	4488	892	24.06 ± 0.01
<i>g</i> ⁺	4804	1265	23.87 ± 0.01
<i>V</i>	5487	954	23.78 ± 0.02
<i>r</i> ⁺	6305	1376	23.84 ± 0.02
<i>i</i> ⁺	7693	1497	23.84 ± 0.03
<i>z</i> ⁺	8978	847	22.56 ± 0.02
<i>z</i> ⁺⁺	9063	1335	22.54 ± 0.01
<i>IB427</i>	4266	207	23.93 ± 0.04
<i>IB464</i>	4635	218	23.76 ± 0.04
<i>IA484</i>	4851	229	23.99 ± 0.04
<i>IB505</i>	5064	231	23.78 ± 0.04
<i>IA527</i>	5261	243	23.93 ± 0.03
<i>IB574</i>	5766	273	24.00 ± 0.05
<i>IA624</i>	6232	300	23.76 ± 0.04
<i>IA679</i>	6780	336	23.43 ± 0.03
<i>IB709</i>	7073	316	23.68 ± 0.03
<i>IA738</i>	7361	324	23.83 ± 0.05
<i>IA767</i>	7694	365	24.38 ± 0.08
<i>IA827</i>	8243	343	24.31 ± 0.07
<i>NB711</i>	7121	72	23.26 ± 0.06
<i>NB816</i>	8150	120	24.11 ± 0.06
<i>HST</i>			
ACS/F814W	8333	2511	23.37 ± 0.01
WFC3/F140W	13923	3933	23.89 ± 0.08
CFHT/WIRCam			
<i>H</i>	16243	2911	23.82 ± 0.26
<i>K_s</i>	21434	3270	24.39 ± 0.44

¹ At the time data reduction was done, GMOS mask ingestion was only available through the v1.10dev version and `gemini_gmos_mask_ingestion` branch. This has since been incorporated in newer official release versions of *PyPeit*.

² <https://github.com/akhostov/EELG1002>

using the brightest object in the mask. *PyPeit* then models the spatial profile of the object and calculates the spatial shift in reference to the first science frame in our 2D coadd list. This is then stacked with weights corresponding to the S/N

of our brightest object. Objects are then extracted using the Horne (1986) optimal extraction algorithm.

3.1.1. Flux Calibration & Slit Loss Corrections

Flux calibration is performed by first reducing our standard star LTT7379 (G0) using the same `PyPeit` reduction as mentioned above. We then used the wavelength-calibrated, reduced spectra to measure the sensitivity curve that converts raw counts into physical flux units. `PyPeit` does this by comparing the observed 1D GMOS spectra against archival spectra drawn, in this case, from the ESO Optical and UV Spectrophotometric Standard Stars library. The final sensitivity curve is then applied to each of our science targets. Atmospheric extinction corrections are applied to both the standard star used in generating the sensitivity curve and the science target spectra taking into account the varying airmass at the time of observation. This is all included in the `PyPeit` scripts that make the sensitivity curve and apply the flux calibration. This was done by using the observatory’s extinction file (in our case, La Silla) and applying the extinction curve as a function of wavelength and air mass associated with the spectra being corrected.

An additional correction is also necessary to account for slit loss (e.g., a fraction of the total flux is lost because the object extends off the slit). Figure 1 shows the configuration of the GMOS slit along with the Subaru / HSC *i* contours demonstrating how a significant fraction of light falls outside the slit. We corrected for this factor using the spatially resolved *HST*/ACS F814W image also shown in Figure 1 and measure the total flux collected along the slit. We then smoothed out the F814W image using a Gaussian kernel with FWHM set to the seeing (0.9'') and again measured the total flux within the 0.5'' slit. We measure 45.6% of the total flux from EELG1002 is lost and correct the 1D spectra by multiplying a factor of 1.456 to take into account the slit loss.

3.2. Spectroscopic Redshift & Emission Line Profile Fitting

We used `PyQSOFit` (Guo et al. 2018) for fitting the profiles of all emission lines observed in the GMOS spectra, which requires an initial estimate of the visually measured spectroscopic redshift ($z = 0.8275$) using `SpecPro` (Masters & Capak 2011). Each detected emission line is fit by a single Gaussian profile with the central wavelength allowed to vary to capture variations in the final measured spectroscopic redshift. Line widths of each emission line are set to be constant among other associated lines within the same atomic species (e.g., FWHMs of the Balmer line are the same from $H\beta$ to $H\eta$). This allows us to deblend lines from different atomic species that are in close wavelength proximity to one another (e.g., $[\text{NeIII}]3968\text{\AA}$ and HeI separated by 2.6\AA ; rest-frame) and are not fully resolved given the GMOS wavelength resolution limit. The $[\text{OII}]3726,3729\text{\AA}$ doublet is also not re-

solved, for which we fit two Gaussians assuming the FWHM from $[\text{OIII}]5007\text{\AA}$ to fit the doublet. Line fluxes are measured by integrating the best-fit Gaussian profiles. We do not include Balmer absorption corrections as such features were not observed (see Figure 2) and are not expected for such a young galaxy as will be shown further in this paper.

Uncertainty measurements are measured by sampling the posterior probability distributions associated with each parameter in the emission line profiles via Markov Chain Monte Carlo (MCMC) using `emcee` (Foreman-Mackey et al. 2013). `PyQSOFit` does this by using the best-fit parameters of each line profile as the initial starting point in the chain perturbed by a small random offset and assuming 100 walkers. To ensure convergence and well-sampling of the true posterior probability distributions, `emcee` keeps track of the autocorrelation time which measures how many steps are required to ensure independent samples are used with the condition that the number of samples is greater than 50 times the autocorrelation time. After several tests, we determined 15000 samples with a 20% burn-in (discard the initial steps) satisfies this criteria. Overall, each emission line detected has an associated probability distribution that will be used throughout this work to measure line ratios and associated uncertainties.

3.3. Velocity Dispersion

The observed velocity dispersion, σ_{obs} , is measured using the best-fit Gaussian emission line profile. We measure the ‘intrinsic’ velocity dispersion, σ_{int} , by:

$$\sigma_{int} = \sqrt{\sigma_{obs}^2 - \sigma_{inst}^2 - \sigma_{th}^2} \quad (1)$$

which subtracts out the effects of instrumental (σ_{inst}) and thermal (σ_{th}) broadening. The latter is measured as $\sigma_{th} = \sqrt{k_B T_e / m_X}$, where k_B is the Boltzmann constant, m_X is the mass of atomic species (e.g., H, O, Ne), and T_e is the electron temperature for which we use our measurement described in §3.4.2 and Table 3. The instrumental broadening is measured using the FWHM of the CuAr arc lines (2.5 pix with $3.88\text{\AA}\text{pix}^{-1}$ resolution).

3.4. Measuring ISM Properties

In this section, we will describe how we use nebular emission line ratios in conjunction with `PyNeb` (Luridiana et al. 2015) to measure key ISM properties. We present the key line ratios with the shorthand notation used in this work and its exact definitions (e.g., lines used) in Table 2.

3.4.1. Dust Extinction

Balmer decrements (e.g., $\text{Ha}/\text{H}\beta$) trace the level of dust extinction within HII regions and are used to dust-correct observed line fluxes when coupled with an assumed dust attenuation curve. The reddening is measured by comparing the

Table 2. Key Line Ratio shorthands and definitions used throughout this paper.

ID	Definition
O3HB	[OIII]5007Å/Hβ
O32	[OIII]5007Å/[OII]3726, 3729Å
Ne3O2	[NeIII]3869Å/[OII]3726, 3729Å
Ne3O3	[NeIII]3869Å/[OIII]5007Å
R2	[OII]/Hβ
R3	([OIII]5007Å + [OIII]4959Å)/Hβ
R23	([OIII]5007Å + [OIII]4959Å + [OII])/Hβ

observed-to-intrinsic Balmer ratios as shown below:

$$E(B - V) = \frac{2.5}{k(H\gamma) - k(H\beta)} \log_{10} \left(\frac{[H\beta/H\gamma]_{\text{obs}}}{[H\beta/H\gamma]_{\text{int}}} \right) \quad (2)$$

coupled with the dust attenuation curve evaluated at the wavelength of each Balmer line used, $k(\lambda)$, for which we assume the Calzetti et al. (2000) attenuation curve. The amount of dust extinction is then measured as $A_\lambda = k(\lambda)E(B - V)$ at any given wavelength. The GMOS spectral coverage does not include H α for which we instead use the next brightest ratio, H β /H γ , to measure $E(B - V)$ and A_λ . The intrinsic line ratio, H β /H γ = 2.11, is determined using PyNeb assuming case B recombination, T_e = 15000 K (electron temperature) and n_e = 100 cm⁻³ (electron density). Varying these assumptions marginally changes the intrinsic ratios and does not affect our dust-extinction measurements. Uncertainties in $E(B - V)$ are measured by each MCMC realization used in the fitting of the emission line profile (see §3.2).

3.4.2. Electron Temperature & Density

The electron temperature is measured using a two-zone HII region model due to [OIII] (doubly ionized oxygen) tracing the (high ionizing) zone closest to the ionizing source and [OII] (single ionized oxygen) being able to trace the outer (low ionizing) zone. Electron temperature of the high ionizing zone, $T_e(\text{O}^{++})$, is measured using the auroral [OIII]4363/[OIII]5007Å line ratio at a fixed n_e = 1000 cm⁻³ and the getTemDen function in PyNeb. The fixed n_e is done arbitrarily as T_e is essentially independent of electron density up to $\sim 10^4$ cm⁻³ (not expected for ISMs of galaxy populations) but is an input in getTemDen.

Measuring the low ionizing zone electron temperature requires O⁺ auroral lines (e.g., [OII]7322,7332Å) which are outside our GMOS coverage. Instead, we estimate O⁺ electron temperature using the Izotov et al. (2006) calibration:

$$t_e(\text{O}^+) = t_e(\text{O}^{++}) \times (2.065 - 0.498t_e(\text{O}^{++})) - 0.577 \quad (3)$$

with $T_e = t_e \times 10^4$ K for both O⁺ and O⁺⁺. This assumes the low metallicity condition described in Izotov et al. (2006)

which is found to be appropriate for EELG1002 given its metal-poor nature (see §4.3 and Table 3).

We measure the electron density, n_e , using the [OII]3726,3729Å doublet which is sensitive to T_e (e.g., can vary from ~ 500 cm⁻³ to ~ 640 cm⁻³ by increasing T_e from 10000 K to 20000 K assuming the [OII] doublet ratio is of order unity.) Therefore, we first measure the electron temperature as described above and then measure n_e using getTemDen function with $T_e(\text{O}^+)$ and observed [OII]3729/[OII]3726Å ratio.

3.4.3. Gas-Phase Abundance

Abundances associated with Oxygen and Neon are measured using PyNeb and its getIonAbundance feature assuming the electron temperatures in both the high and low ionizing zones. Our approach assumes n_e is constant throughout the ionizing zones. Below we describe how the ionic and total abundances are measured.

Oxygen abundance is measured with the formalism:

$$\frac{\text{O}}{\text{H}} \approx \frac{\text{O}^+}{\text{H}} + \frac{\text{O}^{++}}{\text{H}} \quad (4)$$

where additional abundance contribution from O⁺⁺⁺ is not expected to contribute significantly to the overall O/H abundance. Specifically, to have O⁺⁺⁺ requires 54.9 eV and, therefore, we would also expect Helium recombination lines (e.g., HeI4686Å) for which we find no detections in the GMOS spectra. Berg et al. (2018) investigated a $z \sim 2$ lensed source with OIV detection and found that O⁺⁺⁺/H contribution only accounted for a $\sim 5\%$ increase (+0.02 dex) in the total O/H abundance. Therefore, we continue measuring O/H abundance as defined in Equation 4. The O⁺⁺/H abundance is measured using R3 with n_e and $T_e(\text{O}^{++})$ measured in §3.4.2 and O⁺/H is measured using R2, n_e , and $T_e(\text{O}^+)$.

The neon abundance is defined as:

$$\frac{\text{Ne}}{\text{H}} \approx \frac{\text{Ne}^{++}}{\text{H}} \times \text{ICF} \quad (5)$$

where the ionization correction fraction (ICF) traces the relative contribution from other Neon ionization states (e.g., Ne⁺). We adopt the ICF formalism of Izotov et al. (2006):

$$\text{ICF} = 1.365 - 0.385 \frac{\text{O}^{++}}{\text{O}^+ + \text{O}^{++}} + 0.022 \frac{\text{O}^+ + \text{O}^{++}}{\text{O}^{++}} \quad (6)$$

which assumes a low metallicity system (consistent with EELG1002; see Table 3). The Ne⁺⁺/H abundance is measured using the [NeIII]3869Å/Hβ ratio along with our measured n_e and $T_e(\text{O}^{++})$ as [NeIII] requires 41 eV comparable to the 35 eV needed for [OIII] emission. Although EELG1002 has strong [NeIII]3968Å emission (see Figure 2), we do not include it in the abundance measurement due to uncertainties from He blending.

3.4.4. Ionization Parameter

The ionization parameter is defined as:

$$U = \frac{Q_H}{4\pi R_S^2 c n_H} \quad (7)$$

where Q_H is the number of hydrogen ionizing photons per unit time, R_S is the Strömgen radius, c is the speed of light, and n_H is the hydrogen number density (comparable to the electron density, n_e). Essentially, U traces how many ionizing photons are produced within an HII region in comparison to the present number of hydrogen atoms. A higher ionization parameter would signify more ionizing photons and/or fewer hydrogen atoms that can be interpreted as energetic ISM conditions.

O32 is a classical indicator of U as O^{++} requires 35 eV compared to O^+ which requires 13.6 eV such that it is sensitive to the ionization state of gas within HII region. An alternative is the Ne3O2 ratio where Ne^{++} requires ~ 41 eV and is insensitive to dust attenuation (Levesque & Richardson 2014). Coupling of both can also provide insight as to the shape (hardness) of the ionizing spectrum given Ne^{++} has ionization potential ~ 6 eV higher than O^{++} (e.g., Strom et al. 2017; Jeong et al. 2020). Using both diagnostics to directly measure U is limited based on the gas-phase metallicity range used in calibrating the diagnostic (Kewley et al. 2019). As such, we measure U via photoionization modeling included in Bagpipes (Carnall et al. 2018) and Cigale (Boquien et al. 2019).

In making measurements of U , one must be cautious about electron densities assumed given its inverse proportionality. The typical assumption of 100 cm^{-3} can overestimate (underestimate) U if the source of interest has $n_e > 100$ (< 100) cm^{-3} . We take this into account in our spectrophotometric SED fitting (§3.5) by using $n_e = 1000 \text{ cm}^{-3}$ in the older Cloudy model within Cigale (pre-defined grid; §3.5.1) and recompute the Cloudy grid used in Bagpipes (§3.5.2) assuming $n_e = 800 \text{ cm}^{-3}$ consistent with EELG1002 (Table 3).

3.5. Spectral Energy Distribution Fitting

In this section, we describe our SED fitting parameters and assumptions used in both Cigale and Bagpipes where we simultaneously fit both the GMOS spectra and ancillary multi-wavelength photometry (see §2). Although GALEX/FUV and NUV photometry do exist for EELG1002, we chose to disregard it in the SED fitting process given the low spatial resolution as shown in Figure 1 where blending with 2 nearby sources is an issue. The same is true for Spitzer/IRAC photometry. Lastly, all photometry used in the SED fitting process has an additional 10% uncertainty included in quadrature to account for underestimated errors.

Setup files are also made available within the GitHub repository³.

3.5.1. CIGALE

We use Cigale v2022.1 (Boquien et al. 2019; Yang et al. 2022a), a template grid-based SED fitting code, and provide a brief overview of assumptions made in the SED fitting process which are highlighted in Table 7. Both photometry and line fluxes measured from the GMOS spectra are included in the SED fitting process. Briefly, we assume a Bruzual & Charlot (2003) stellar population synthesis model coupled with a Chabrier (2003) IMF and consider stellar metallicities within the range of 0.005 and $1 Z_\odot$. Nebular emission is modeled using the Inoue (2011) templates which were generated using Cloudy v13.01 (Ferland et al. 2013) with U considered in the range of -3.0 to -1.0 . Gas-phase metallicity is fixed to 0.001 (closest to our best metallicity measurement; Table 3). Cigale only allows for three different fixed values for n_e for which we assume 1000 cm^{-3} given our measured n_e (see Table 3 and §3.4.2). Both f_{esc} (LyC escape fraction) and f_{dust} (fraction of LyC photons absorbed by dust) are fixed to 0% in the nebular emission modeling; however, we do note that there is the possibility of a nonzero f_{esc} given GALEX/FUV detection (blended with 2 nearby sources) and we discuss the prospects of LyC escape for EELG1002 in §5.5. All emission lines in the model have fixed observed FWHM set to 400 km s^{-1} , consistent with our observations (Table 4). $E(B-V)$ is fixed to 0 mag given $H\beta/H\gamma$ (see Table 3).

We assume a delayed- τ star formation history with a recent burst. The main/old stellar population is considered with e-folding time, τ_{main} , of 50 Myr to 7.5 Gyr and ages of 50 Myr to 6.6 Gyr. Setting $\tau_{main} > 6.6$ Gyr (age of Universe at $z = 0.8275$) would describe a continuously rising SFH. The young stellar population formed in the recent burst is modeled with e-folding time, τ_{burst} , between 1 and 100 Myr with ages between 1 to 50 Myr. The contribution of stellar mass formed in the recent burst towards the stellar mass of the galaxy, f_{burst} , is considered between 0 and 99%, where the latter is the maximum allowed in Cigale and is interpreted as a galaxy for which the total stellar mass was formed recently in a single burst of star formation.

3.5.2. Bagpipes

We use Bagpipes (Carnall et al. 2018), a Bayesian spectrophotometric SED fitting suite, to take advantage of several features: nonparametric star formation history (SFH) modeling, inclusion of binary stellar populations, updated photoionization models from Cloudy v17 (Ferland et al. 2017), and direct fitting to the 1D spectra (Cigale only fits to pro-

³ <https://github.com/akhostov/EELG1002>

vided line fluxes). Bagpipes uses MultiNest (Feroz & Hobson 2008; Feroz et al. 2009, 2019), a nested sampling package that samples the parameter space given a likelihood, and bayesian inference to measure best-fit properties. Table 8 highlights our defined parameter space and all setup files are available via our GitHub repository. Briefly, we use BPASS v2.2.1 (Stanway & Eldridge 2018) which includes binary stellar populations with an assumed broken power law IMF with a slope of -1.35 ($0.1 - 0.5 M_{\odot}$) and -2.35 ($0.5 - 300 M_{\odot}$). The shallower slope at low stellar masses allows for an increased contribution of the older, low-mass stellar population compared to Chabrier (2003) IMF (exponentially cuts off at $0.1 - 1 M_{\odot}$). Nebular metallicity is fixed to our gas-phase metallicity shown in Table 3 while the stellar metallicity is a free parameter. Reddening is also set to 0 mag given our measured Balmer Decrement suggests no dust extinction. Templates for the nebular component are recomputed with Cloudy v17.03 using the default BPASS stellar grid provided in Bagpipes to cover $\log_{10} U = -4$ to -1 in order to consider cases of extreme energetic ISM conditions. To ensure reliable ionization parameter measurements, we recompute the Cloudy grid to also assume $n_e = 800 \text{ cm}^{-3}$ consistent with our source (see Table 3).

The non-parametric SFH is modeled using the Leja et al. (2019) continuity formalism within Bagpipes which separates the stellar mass contribution within inputted time bins. We follow the time bin spacing used in past non-parametric SFH modeling studies (e.g., Leja et al. 2017, 2019; Tacchella et al. 2022; Tang et al. 2022): 0, 3, 10, 30, 100, 300, 1000, 3000, and 6000 Myr. These are logarithmically spaced equally (~ 0.5 dex) except for the 3000 – 6000 Myr bin which is limited by the age of the Universe. Shorter time bins gauge how rapidly the recent burst of star formation occurred and are constrained primarily by the multiple strong Balmer line detections tracing instantaneous star formation activity while longer time bins factor in past star formation that formed the older stellar population.

3.6. Measuring Equivalent Width

Equivalent width (EW) is measured as the ratio between emission line flux (§3.2) and its associated continuum flux density (§3.5). The latter is measured using the best-fit Cigale and Bagpipes SEDs by first masking out the emission line of interest. We then select continuum flux densities within 2 windows: one bluewards and the other redwards of the emission line. Both windows are 10\AA (rest) in width and are placed $\pm 10\text{\AA}$ (rest) from the emission line center. We place the windows for [OIII]5007Å and [OIII]4959 at 15\AA away from the line center and with a width of 20\AA given how strong the lines are (e.g., ensuring we are not probing the line profile wings in the continuum flux density measurement). In the case of H γ , we set the red window to be

35\AA from center (10\AA width) to ensure we do not include the nearby [OIII]4363Å line for which that line also has its blue window placed closer (-6\AA from line center and extending to -15\AA). [NeIII]3869 also has the red window placed 35\AA from center (width 10\AA) to ensure H8 emission is not included in the window. The same is true for H8 with the blue window set to -35\AA from line center.

Using the continuum flux densities measured within each window, we interpolate the SED shape between both windows and measure the flux density about the emission line center. We then take the ratio of the emission line flux and the determined continuum flux density and measure the equivalent width of the line which are shown in Table 4 and labeled based on whether the best-fit Cigale or Bagpipes SED was used in determining the continuum flux density.

3.7. Ionizing Photon Production Efficiency

The ionizing photon production efficiency, ξ_{ion} , traces how well a galaxy can produce ionizing photons (e.g., $> 13.6 \text{ eV}$ that can ionize H1) and is defined as:

$$\xi_{ion} = \frac{Q_H}{L_{UV}^{int}} \quad (8)$$

where Q_H represents the production rate of hydrogen ionizing photons and L_{UV}^{int} is the intrinsic, rest-frame, dust-corrected 1500\AA continuum luminosity. The definition of ξ_{ion} is slightly varied where we refer the reader to §3.2 of Chevallard et al. (2018) for a detailed discussion. One definition typically cited as ξ_{ion}^* uses the monochromatic UV luminosity attributed only to the stellar continuum and ignores the emission and absorption caused by neutral and ionized gas. Another definition cited as ξ_{ion}^{HII} incorporates the nebular and stellar continuum in measuring the 1500\AA monochromatic luminosity (L_{UV}^{HII}). We adopt this definition throughout this paper and use both ξ_{ion}^{HII} and ξ_{ion} interchangeably unless otherwise clarified if we are referring to another definition (e.g., ξ_{ion}^*).

We use the best-fit combined stellar and nebular continuum fits from Cigale and Bagpipes to measure L_{UV} using a tophat filter centered at 1500\AA with a width of 100\AA . We use the Leitherer & Heckman (1995) calibration:

$$Q_H = 2.1 \times 10^{12} L_{int}(H\beta) [\text{s}^{-1}] \quad (9)$$

to measure the ionizing photon production rate, Q_H , with H β luminosity from our observed GMOS spectra. This assumes a Lyman Continuum escape fraction $f_{esc} = 0$ and represent the maximum Q_H possible based on the calibration. Given that Balmer Decrements show $E(B - V) \sim 0$ mag, we do not apply any dust correction.

3.8. Galaxy Size & Dynamical Mass Measurement

We use archival *HST* ACS/F814W to measure the rest-frame $\sim 4500\text{\AA}$ galaxy size. A single Sersic profile is assumed and fitted to the F814W image using *pysersic* (Pasha & Miller 2023): a public package that uses Bayesian inference to fit Sersic profiles to galaxy images. We also assume a flat background around EELG1002 which is simultaneously fit during the Sersic profile fitting. Assumed priors are the default in *pysersic*. The effective/half-light radius, r_e , has a truncated normal prior centered at 3.52 pixels with σ of 3.75 pixels and a minimum cutoff at 0.5 pixels. The Sersic index, n , is set to a uniform prior between 0.65 and 8. The posterior for both variables is measured using a No U-turn Sampler (NUTS, Hoffman et al. 2014) and is used to measure the uncertainties.

The dynamical mass is measured based on the half-light radius and intrinsic velocity dispersion (§3.3) and traces all baryonic matter within the galaxy: stellar, gas, dust, and dark matter. Given that we have measurements of stellar mass from our SED fitting and that EELG1002 has relatively no dust (Table 3), the dynamical mass compared to the stellar mass provides a tracer of how much gas and dark matter resides within EELG1002. The dynamical mass is defined as:

$$M_{\text{dyn}} = C \frac{\sigma_{\text{int}}^2 r_e}{G} \quad (10)$$

where r_e is the effective radius, G is the gravitational constant, σ_{int} is the intrinsic velocity dispersion (corrected for instrumental and thermal broadening; see §3.3), and C is the scaling factor. We use the $H\beta$ σ_{int} as shown in Table 4. The scaling factor is dependent on the mass distribution and velocity field of the galaxy and could range from $C \sim 1 - 5$ (Erb et al. 2006). We follow Maseda et al. (2013) which measured dynamical masses for EELG populations at $z \sim 2$ and assumed $C = 3$. However, we also incorporate the range of $C \sim 1 - 5$ in our uncertainties by uniformly sampling C between 1 and 5 and measuring the dynamical mass. This provides for a conservative estimate on the possible range in dynamical mass.

4. RESULTS

4.1. Record Breaking High EW, Low Mass Extreme Emission Line Galaxy at $z \sim 0.8$

EELG1002 ($\alpha = 10 : 00 : 32.304$, $\delta = +2 : 51 : 11.351$) is a uniquely low-mass, high EW emission line galaxy with numerous emission line detections, as shown in the top panel of Figure 2, that, in conjunction with the wealth of multi-wavelength ancillary photometry, provides us a great deal of information in regards to its star-formation and ISM conditions. We present redshift, line flux, EW, and velocity dispersion measurements for each line in Table 4. We find a spectroscopic redshift in the range of $z_{\text{spec}} \sim 0.8273$ and 0.8276 depending on which line is used ($H\beta$, $[\text{OIII}]5007\text{\AA}$,

Table 3. Measured ISM properties of EELG1002 with the methodology described in §3.4.

ISM Property	Measurement
Electron Temperature & Density	
$T_e(\text{O}^{++})$ (K)	19507^{+1620}_{-1548}
$T_e(\text{O}^+)$ (K)	15536^{+91}_{-297}
n_e (cm^{-3})	779^{+927}_{-487}
Oxygen Abundance	
$12 + \log_{10}(\text{O}^{++}/\text{H})$	$7.454^{+0.081}_{-0.074}$
$12 + \log_{10}(\text{O}^+/\text{H})$	$6.679^{+0.067}_{-0.051}$
$12 + \log_{10}(\text{O}/\text{H})$	$7.522^{+0.074}_{-0.065}$
$Z_{\text{gas}}(Z_{\odot})$	$0.068^{+0.013}_{-0.009}$
Neon Abundance	
$12 + \log_{10}(\text{Ne}^{++}/\text{H})$	$6.897^{+0.092}_{-0.085}$
$12 + \log_{10}(\text{Ne}/\text{H})$	$6.923^{+0.090}_{-0.082}$
$\text{ICF}(\text{Ne}^{++})$	$1.061^{+0.011}_{-0.008}$
$\log_{10}(\text{Ne}/\text{O})$	$-0.600^{+0.027}_{-0.027}$
Ionization Parameter – $\log_{10} U$	
Bagpipes + BPASS	$-1.96^{+0.06}_{-0.06}$
Cigale + BC03	-2.23 ± 0.06
Balmer Decrement	
$H\beta/\text{H}\gamma$	$1.940^{+0.142}_{-0.130}$
$E(B - V)$ via $H\beta/\text{H}\gamma$ (mag)	$0.00^{+0.00}_{-0.00}$
Line ratios	
O3HB	$4.919^{+0.242}_{-0.222}$
O32	$8.917^{+0.438}_{-0.444}$
R2	$0.554^{+0.037}_{-0.034}$
R3	$6.541^{+0.323}_{-0.303}$
R23	$7.091^{+0.349}_{-0.320}$
$[\text{OIII}]_{4363\text{\AA}}/[\text{OIII}]_{5007\text{\AA}}$	$0.032^{+0.004}_{-0.004}$
Ne3O2	$1.076^{+0.069}_{-0.065}$
Ne3O3	$0.121^{+0.006}_{-0.005}$

and $[\text{NeIII}]3869\text{\AA}$). The discrepancies are well within 1σ error bars and could arise simply due to uncertainties within the wavelength calibration and limiting resolution of the GMOS R150 grating. Throughout this work, we quote the spectroscopic redshift as $z_{\text{spec}} \sim 0.8275$ which is the average of the three different measurements.

Figure 2 shows all the multi-wavelength photometry associated with EELG1002 and our best-fit Cigale and Bagpipes SEDs. The photometry alone shows the presence of nebular emission line contribution in the narrowband, intermediate band, and broadband photometries (e.g., Subaru SuprimeCam and HSC z -band is dominated by the presence of $[\text{OIII}]+H\beta$) which would suggest high EW emission

Table 4. Emission Line Properties for all detected lines in the GMOS spectra. Line flux and velocity dispersions, σ , are measured using PyQSOFit with FWHM fixed based on H β , [OIII], and [NeIII] for the Hydrogen, Oxygen, and Neon atomic species, respectively. The spectroscopic redshifts are also based on the brightest line of each species and is found to be consistent with $z \sim 0.8275$ within 1σ . Rest-frame Equivalent Width (EW₀) measurements use the best-fit SED (Cigale and Bagpipes) for measuring the continuum flux density about the emission line wavelength. Observed velocity dispersion, σ_{obs} , is based on the best-fit FWHM from the emission line profile. Intrinsic velocity dispersion, σ_{int} , corrects σ_{obs} for instrumental and thermal broadening (§3.3).

Line	z_{spec}	Observed Line Flux (10^{-17} erg s $^{-1}$ cm $^{-2}$)	EW ₀ (Cigale) (10^{-17} erg s $^{-1}$ cm $^{-2}$)	EW ₀ (Bagpipes) (Å)	σ_{obs} (km s $^{-1}$)	σ_{int} (km s $^{-1}$)
Balmer Lines						
H β	$0.8273^{+0.0005}_{-0.0005}$	$18.74^{+0.87}_{-0.87}$	$472.84^{+22.04}_{-22.03}$	$403.64^{+18.81}_{-18.81}$	192^{+7}_{-6}	131^{+9}_{-10}
H γ	—	$9.65^{+0.49}_{-0.48}$	$187.12^{+9.41}_{-9.26}$	$157.02^{+7.90}_{-7.77}$	—	—
H δ	—	$4.06^{+0.32}_{-0.32}$	$71.93^{+5.65}_{-5.64}$	$57.31^{+4.50}_{-4.49}$	—	—
H ϵ	—	$2.26^{+0.38}_{-0.38}$	$36.84^{+6.24}_{-6.23}$	$29.49^{+5.00}_{-4.99}$	—	—
H ζ +HeI3889Å	—	$0.71^{+0.33}_{-0.32}$	$10.50^{+4.88}_{-4.72}$	$8.41^{+3.91}_{-3.78}$	—	—
H η	—	$3.02^{+0.31}_{-0.31}$	$46.83^{+4.74}_{-4.80}$	$37.36^{+3.78}_{-3.83}$	—	—
Oxygen Lines						
[OIII]5007Å	$0.8276^{+0.0005}_{-0.0005}$	$92.15^{+0.63}_{-0.64}$	$2438.63^{+16.75}_{-17.05}$	$2039.37^{+14.01}_{-14.25}$	145^{+1}_{-1}	52^{+3}_{-3}
[OIII]4959Å	—	$30.43^{+0.39}_{-0.41}$	$786.47^{+10.16}_{-10.69}$	$658.25^{+8.50}_{-8.95}$	—	—
[OIII]4363Å	—	$2.97^{+0.40}_{-0.40}$	$59.93^{+8.01}_{-8.08}$	$48.02^{+6.42}_{-6.47}$	—	—
[OII]3726,3729Å	—	$10.28^{+0.46}_{-0.46}$	$154.89^{+6.88}_{-6.88}$	$126.57^{+5.63}_{-5.62}$	—	—
[OII]3726Å	—	$5.30^{+0.74}_{-0.75}$	$79.11^{+11.03}_{-11.20}$	$67.83^{+9.46}_{-9.60}$	—	—
[OII]3729Å	—	$4.98^{+0.73}_{-0.73}$	$68.75^{+10.11}_{-10.08}$	$59.09^{+8.69}_{-8.67}$	—	—
Neon Lines						
[NeIII]3869Å	$0.8275^{+0.0006}_{-0.0006}$	$11.06^{+0.49}_{-0.47}$	$159.79^{+7.01}_{-6.84}$	$131.48^{+5.77}_{-5.63}$	232^{+12}_{-11}	141^{+19}_{-20}
[NeIII]3968Å	—	$3.42^{+0.00}_{-0.00}$	$55.54^{+0.00}_{-0.00}$	$44.65^{+0.00}_{-0.00}$	—	—

lines. Cigale (green) and Bagpipes (red) SEDs are for the most part consistent in showing strong nebular emission line features, but vary in several key areas. Both Cigale and Bagpipes show a strong inverse Balmer jump and slightly increasing UV slope consistent with the presence of young stellar populations.

We find EELG1002 has a stellar mass of $(2.75^{+1.61}_{-1.77}) \times 10^8 M_{\odot}$ (Bagpipes) and $(1.14 \pm 0.44) \times 10^8 M_{\odot}$ (Cigale). Using the continuum fluxes as described in §3.6, we find EELG1002 has significantly strong EWs as shown in Table 4. The combined rest-frame [OIII]+H β EW for EELG1002 is 3101^{+25}_{-25} Å (Bagpipes) and 3697^{+30}_{-30} Å (Cigale) which is significantly high for a $z \sim 0.8$ emission line galaxy. To understand how ‘extreme’ EELG1002 requires that we take this within the context of how elevated the [OIII]+H β EW is in comparison to typical star-forming galaxies at the same stellar mass and redshift. Figure 3 shows the typical EWs of emission line galaxies at a given stellar mass and redshift from $z \sim 0.8$ to 3.2 measured from narrowband-selected [OIII] emitters (Khostovan et al. 2016). We find that EELG1002 lies 32 (Bagpipes) to 36 (Cigale) times above the typical [OIII]+H β EWs at $z \sim 0.8$ placing this well above the typical range of EWs of star-forming galaxies at similar redshift and stellar mass.

In both Cigale- and Bagpipes-measured continuum and stellar mass, EELG1002 is also ‘extreme’ relative to typical $z \sim 3.2$ (Khostovan et al. 2016) and even $z \sim 3 - 7$ [OIII] emitters observed recently with *JWST* via EIGER (Matthee et al. 2023) and JADES (Boyett et al. 2024). EELG1002 is also consistent in terms of its EW with $z \sim 0$ confirmed $z < 0.5$ LyC Leakers (e.g., Izotov et al. 2016, 2018, 2021b) and Blueberries (Yang et al. 2017b) (compact, high EW, extreme emission line galaxies at $z \sim 0$) and is even more ‘extreme’ in its [OIII]+H β EW compared to known high- z LyC leakers. For example, *Ion2* (de Barros et al. 2016) has [OIII]+H β EW ~ 1103 Å which is $\sim 2.2\times$ higher than typical $z \sim 3$ [OIII] emitters. BOSS-EUVLG1 (Marques-Chaves et al. 2020) has [OIII]+H β EW ~ 1125 Å which is $\sim 3.7\times$ higher than typical $z \sim 2.2$ EWs.

Overall, EELG1002 has $\sim 32 - 36\times$ higher [OIII]+H β EW compared to the typical EW of a star-forming galaxy at similar stellar mass and redshift making it a potentially record-breaking system in this regard. It also has EWs at or larger than the typical EWs currently observed by high- z studies with *JWST* making it uniquely placed as an analog of high- z galaxies and provides an opportunity given the wealth of emission lines detected in the GMOS spectra to investigate star-formation and ISM properties in great detail.

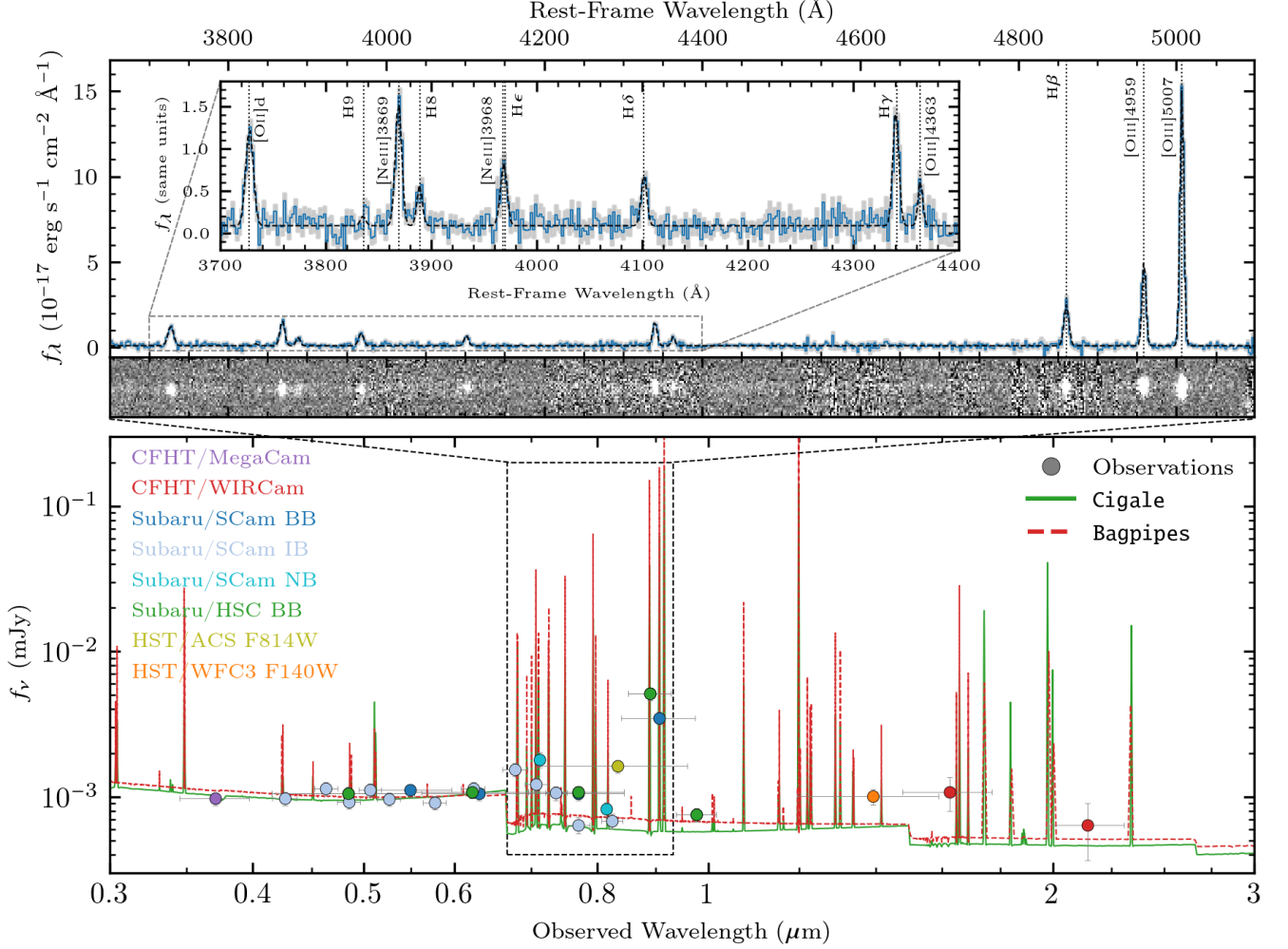


Figure 2. *Top:* Reduced GMOS spectra of EELG1002 highlighting multiple emission line detections securing the spectroscopic redshift with the fitted emission line spectrum (*black dashed line*). Strong [OIII]5007Å relative to [OII]3727Å emission along with comparable [NeIII]3869Å and [OII] emission highlight the highly energetic ISM. [OII]4363Å detection allows for direct- T_e abundance measurements confirming the low-metallicity nature. *Bottom:* Multiwavelength photometry and best-fit SEDs for EELG1002 with Cigale (*green*) and Bagpipes (*red*). Strong [OIII]+H β color excess is clearly observed in Subaru/HSC and SCam *i* indicative of high EWs. HST F814W also shows an excess although not as sensitive given the wider wavelength coverage. Subaru intermediate and narrowbands are also affected by strong nebular emission line features. Cigale and Bagpipes are in relative agreement with slight differences. We note stellar population, IMF, and SFH modeling assumptions may be driving these minor differences.

4.2. No Evidence of AGN component

Although EELG1002 has uniquely high [OIII]+H β EW given its redshift and stellar mass, it does raise the question: *is such strong nebular emission driven by an active galactic nuclei (AGN)?* We address this question and possibility using all the available evidence that we have on hand.

We first investigate the GMOS spectra for signatures of broad line emission that could be an indication of Type 1 AGN (‘BL-AGN’, FWHM > 1000 km s⁻¹; e.g., [Stirpe 1990](#); [Ho et al. 1997](#)). However, as shown in Figure 2, we find no evidence for a broad line component in any of the observed emission lines. Furthermore, the observed velocity dispersion reported in Table 4 range from 145 to 232 km s⁻¹ and

correcting for instrumental resolution and thermal broadening reduces the velocity dispersion to between 52 and 141 km s⁻¹ which is well below the > 1000 km s⁻¹ FWHM typically observed in BL-AGN (e.g., [Genzel et al. 2014](#)).

We also consider the possibility of a potentially strong ionizing radiation spectrum (see §4.4) that could produce strong ionization lines such as [NeV]3426Å (requires ~ 94 eV) indicative of an AGN. However, we find no evidence within the GMOS spectra for the presence of [NeV] emission. We also inspect *Chandra*-COSMOS ([Civano et al. 2016](#); [Marchesi et al. 2016](#)) and *XMM* imaging (PI: G. Hasinger; e.g., [Hasinger et al. 2007](#)) and find no hard and soft X-ray detections.

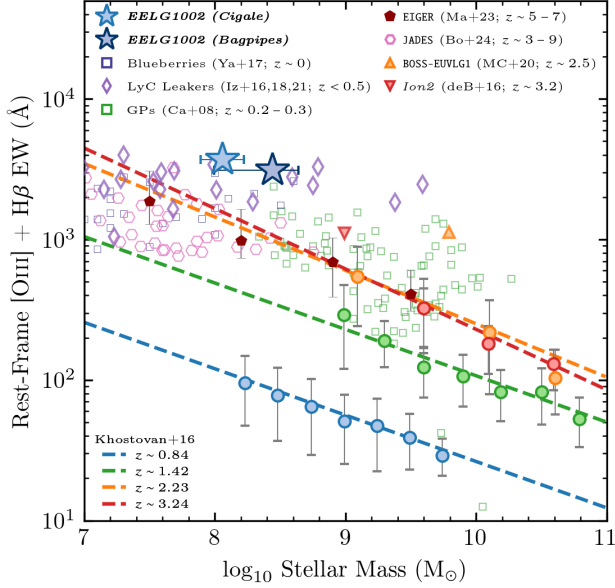


Figure 3. The rest-frame [OIII]+H β EW – stellar mass anti-correlation. EELG1002 is shown as a *star* with *dark blue* using Bagpipes and *light blue* for Cigale for the continuum flux density in measuring [OIII]+H β EW. We find EELG1002 is a uniquely ‘extreme’ ELG with [OIII]+H β EW $\sim 32 - 36\times$ higher compared to the typical [OIII]+H β EW at $z \sim 0.8$ (blue line; Khostovan et al. 2016) and somewhat higher than the typical EW at $z \sim 3 - 9$ (Khostovan et al. 2016; Matthee et al. 2023; Boyett et al. 2024). EELG1002 also has EW higher than Blueberries (Yang et al. 2017b), Green Peas (Cardamone et al. 2009), the $z \sim 2.5$ intense starburst BOSS-EUVLG1 (Marques-Chaves et al. 2020), and the $z \sim 3.2$ LyC emitter Ion2 (de Barros et al. 2016). EELG1002 is consistent with local LyC leakers (Izotov et al. 2016, 2018, 2021b) and we do discuss the potential of LyC escape further in this study. Overall, EELG1002 is a uniquely rare and ‘extreme’ ELG with EWs somewhat more extreme than EoR-era galaxies.

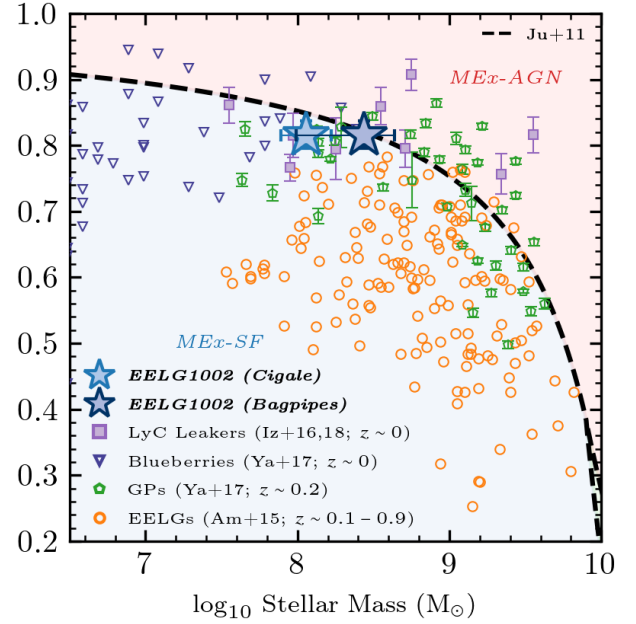


Figure 4. Mass Excitation (MEx) diagram for SFG/AGN classification where EELG1002 is found to have [OIII]/H β ratios and stellar mass consistent with star-forming galaxies. Bagpipes-derived stellar mass is near the boundary; however, this can also be due to the different IMF assumed. [OIII]/H β ratios in conjunction with its low direct T_e measured metallicity is consistent with star-forming galaxies with low [NII]/H α in the BPT diagram (Pettini & Pagel 2004; Marino et al. 2013). EELG1002 also has [OIII]/H β ratios consistent with Blueberries (Yang et al. 2017b) and Green Peas (Yang et al. 2017c). Based on this diagnostic, EELG1002 shows no evidence of an AGN component.

We lastly use the star-forming/AGN classification diagnostic – Mass-Excitation diagram (MEx; Juneau et al. 2011). MEx is very similar to BPT (Baldwin et al. 1981) where instead of [NII]/H α , the diagnostic uses the mass-metallicity relation traced via [NII]/H α to convert the BPT into a $R3$ – stellar mass diagnostic. Figure 4 shows that EELG1002 lies entirely within the star-forming galaxy classification region for the Cigale-measured stellar mass which assumes the same Chabrier (2003) IMF used in the MEx diagram. Bagpipes-measured stellar mass also falls within the star-forming galaxy classification but the upper stellar mass uncertainty does place it slightly within the AGN classification region; however different IMF assumptions between Bagpipes and the MEx classification must be considered as well. Furthermore, [OIII]/H β ratio in conjunction with the low direct T_e metallicity (e.g., low [NII]/H α) is consistent with metal-poor star-forming galaxies within the classic BPT diagram.

Given the available data, we conclude that there is no evidence for the presence of AGN activity within EELG1002 and that the emission lines are most likely driven by star-formation processes. This does not necessarily mean that an AGN is not fully present within EELG1002. One potential possibility is an IR AGN; however, due to the blending of *Spitzer*/IRAC photometry and the lack of spatially resolved *JWST* NIRC2 and MIRI imaging, we can not assess if there is a dusty AGN in EELG1002. Overall, we find no evidence based on the available data that would support an AGN component although future infrared imaging could shed light on the possibility of a dusty AGN component.

4.3. Extremely Metal-Poor, Chemically Unevolved System Consistent with $z \gtrsim 5$ Galaxies

One key feature of the GMOS spectra is the clear $\sim 7.4\sigma$ detection of the auroral [OIII]4363Å emission line which enables direct electron temperature (§3.4.2) and oxygen abundance measurements (§3.4.3). We find EELG 1002 is quite metal poor with $12+\log_{10}(\text{O}/\text{H}) = 7.52 \pm 0.07$ ($Z_{\text{gas}} = 0.068^{+0.013}_{-0.009} Z_{\odot}$ assuming solar gas-phase metallicity ($12 +$

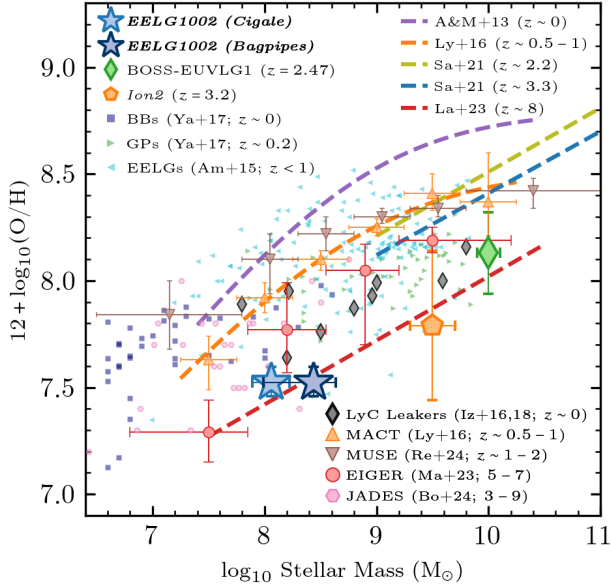


Figure 5. Mass – Metallicity Relation (MZR) with measured relations at $z \sim 0$ (Andrews & Martini 2013), $z \sim 0.5 - 1$ (Ly et al. 2016), $z \sim 2.2 - 3.3$ (Sanders et al. 2021), and $z \sim 8$ (Langeroodi et al. 2023). EELG1002 is found to have $12 + \log_{10}(\text{O}/\text{H})$ below $z < 1$ EELGs (Amorín et al. 2015), Blueberries (Yang et al. 2017b), and Green Peas (Yang et al. 2017c) at fixed stellar mass. Both Cigale and Bagpipes stellar mass measurement places EELG1002 highly consistent with $z \sim 5 - 9$ galaxies at similar stellar mass (Matthee et al. 2023; Langeroodi et al. 2023; Boyett et al. 2024). Similar to EELG1002, Local LyC leakers (Izotov et al. 2016, 2018), *Ion2* (de Barros et al. 2016), and BOSS-EUVLG1 (Marques-Chaves et al. 2020) are consistent with high- z MZR but with higher stellar mass and $12 + \log_{10}(\text{O}/\text{H})$ suggesting past star formation and chemical enrichment periods. EELG1002 is found to have both low-mass and low metallicity consistent with high- z MZR suggesting a chemically-unevolved system that could be undergoing a first bursty phase of star-formation activity as expected of high- z galaxies (e.g., Cohn et al. 2018).

$\log_{10}(\text{O}/\text{H}) = 8.69$; Asplund et al. 2021). This is also consistent with the $R23 - \text{O32}$ calibration of Jiang et al. (2019) which is based on direct T_e measurements using strong emission line emitters where we find $12 + \log_{10}(\text{O}/\text{H}) \sim 7.57$.

In comparison to measured mass-metallicity relations (MZR), we show in Figure 5 that EELG1002 is well below the $z \sim 0$ (Andrews & Martini 2013), $z \sim 0.5 - 1$ (MACT, Ly et al. 2016), and $z \sim 2 - 3$ (Sanders et al. 2021) MZR. EELG1002 is also lower in metallicity compared to known analogs of high- z galaxies such as Blueberries (Yang et al. 2017b), Green Peas (Yang et al. 2017c), and $0.1 < z < 1$ EELGs (Amorín et al. 2015).

Using both Cigale- and Bagpipes-measured stellar mass, we find EELG1002 is in strong agreement with the $z \sim 8$ MZR (Langeroodi et al. 2023), $5 < z < 7$ EIGER (Matthee et al. 2023) and $3 < z < 9$ JADES measurements (Boyett

et al. 2024). In comparison to known local LyC leakers (Izotov et al. 2016, 2018), EELG1002 is found to be slightly metal-poor at similar stellar mass. However, both EELG1002 and local LyC leakers are consistent with both EIGER and Langeroodi et al. (2023) MZR. Furthermore, the $z \sim 3.2$ LyC leaker *Ion2* is also consistent with the $z \sim 8$ MZR although at higher stellar mass and metallicities. The same is found for the intense starburst BOSS-EUVLG1 (Marques-Chaves et al. 2020) which could signify some chemical enrichment has already occurred after a period of intense star-formation activity leading to higher stellar mass and metallicities.

However, EELG1002 is significantly lower in stellar mass and gas-phase metallicity in comparison to *Ion2* and BOSS-EUVLG1 and may be similar to the chemically unevolved conditions expected of galaxies in the early Universe. EELG1002, as will be discussed further in §4.6, is also undergoing an intense period of star formation activity with $\text{H}\beta$ -measured SFR of $7.7 \pm 0.4 M_{\odot} \text{ yr}^{-1}$ with a mass doubling time scale of $\sim 15 - 35$ Myr (see Table 6). This would suggest conditions where star-formation activity recently occurred but did not have time yet to chemically enrich its ISM. In that regard, EELG1002 is potentially an analog of what conditions were like within the $z > 6$ galaxies.

4.4. Energetic ISM Conditions & Harder Ionizing Radiation Field

As shown in the top panel of Figure 2, EELG1002 has strong $[\text{OIII}]5007\text{\AA}$ emission with $\sim (9.2 \pm 0.6) \times 10^{-16} \text{ erg s}^{-1} \text{ cm}^{-2}$ in line flux and moderate $[\text{OII}]$ emission (Table 4) with a measured O32 ratio of $8.92^{+0.44}_{-0.44}$ indicative of energetic conditions (see §4.4). Based on our spectrophotometric SED fitting described in §3.5, we find ionization parameters of $\log_{10} U = -2.23 \pm 0.06$ (Cigale) and $-1.96^{+0.06}_{-0.06}$ (Bagpipes) as shown in Table 3. The discrepancy is most likely attributed to differences in assumed n_e (default in Cigale was 1000 cm^{-3} versus recomputed Cloudy grid in Bagpipes assuming $n_e = 800 \text{ cm}^{-3}$) and the inclusion of binary populations in Bagpipes via BPASS where young hot, massive stars live for longer periods of time allowing for harder ionizing spectra.

Qualitatively, both Cigale and Bagpipes suggests EELG1002 has ionization parameters that would suggest highly energetic conditions within the ISM. The energetic ionization state is aided by the low metallicity conditions described in §4.3 where essentially the number of metal coolants is quite low allowing for higher gas temperatures as we found using $[\text{OIII}]4363\text{\AA}$ ($T_e \sim 19500 \text{ K}$; Table 3). EELG1002 also has $n_e = 779^{+927}_{-487} \text{ cm}^{-3}$ which is higher than typical electron densities at similar redshift ($\sim 20 - 100 \text{ cm}^{-3}$; e.g., Kaasinen et al. 2017; Swinbank et al. 2019; Davies et al. 2021) and is consistent with $z > 5$ galaxies ($> 200 \text{ cm}^{-3}$;

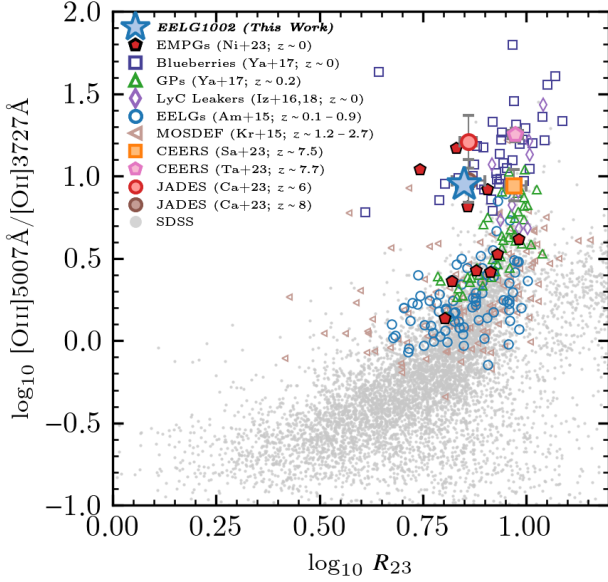


Figure 6. Ionization and Excitation properties. EELG1002 is found to have O32 and R23 well above SDSS (Thomas et al. 2013), EELGs (Amorín et al. 2015), Green Peas (Yang et al. 2017c), and $z \sim 2$ star-forming galaxies (MOSDEF; Kriek et al. 2015). We find EELG1002 has line ratios most consistent with few EMPGs (Nishigaki et al. 2023), Blueberries (Yang et al. 2017b), and high- z stacks from CEERS (Sanders et al. 2023; Tang et al. 2023) and JADES (Cameron et al. 2023). This highlights how EELG1002 has ionization and excitation conditions consistent with EoR-era galaxies making EELG1002 a unique analog in this regard.

e.g., Isobe et al. 2023). Based on Equation 7, this would suggest for elevated levels of hydrogen ionizing photons.

Figure 6 shows the O32 (tracer of ionization parameter) and R23 (indicator of gas-phase metallicity) ratios for EELG1002 along with measurements including SDSS DR12 (Thomas et al. 2013), $z \sim 0$ Extremely Metal Poor Galaxies (EMPGs; Nishigaki et al. 2023), Blueberries (Yang et al. 2017b), Green Peas (Yang et al. 2017c), local LyC leakers (Izotov et al. 2016, 2018), EELGs (Amorín et al. 2015), $z \sim 1 - 3$ MOSDEF (Kriek et al. 2015), $z \sim 7.5$ CEERS (Sanders et al. 2023; Tang et al. 2023), and $z \sim 6 - 8$ JADES (Cameron et al. 2023). We find EELG1002 has O32 and R23 ratios consistent with local Blueberries, local LyC leakers, as well as several EMPGs. It is also consistent with stack measurements from JADES at $z > 6$ highlighting how EELG1002 has both ionization and excitation properties consistent with typical star-forming galaxies in the high- z Universe.

Given the high O32, we can conclude from Figure 6 that EELG1002 has a highly energetic ISM. However, O32 can also be influenced by the incident radiation field shape. Sanders et al. (2016) showed using photoionization modeling that O32 increases at fixed U with harder ionizing radiation field modeled as a simple blackbody spectrum (e.g., presence

of young, hot massive stars). In the case of EELG1002, we can use the Ne3O2 line ratio to gauge the shape of the ionizing radiation field as Ne^{++} requires an ionization potential of 41 eV and, therefore, traces a higher energy regime compared to O^{++} (~ 35 eV). Figure 7 shows the Ne3O2 versus O32 line ratios for EELG1002 along with measurements including $z \sim 1 - 2$ CLEAR (Papovich et al. 2023), $z \sim 1$ HALO7D (Pharo et al. 2023), $z \sim 1 - 3$ MOSDEF (Jeong et al. 2020), and $z \sim 2 - 3$ KBSS (Strom et al. 2017). We find EELG1002 has Ne3O2 and O32 line ratios well above the typical $z \sim 1$ galaxies (e.g., Pharo et al. 2023) and is more consistent with both high- z galaxies (e.g., Cameron et al. 2023; Tang et al. 2023) and local ‘extreme’ systems (e.g., Izotov et al. 2016, 2018; Yang et al. 2017b). Figure 7 also shows that EELG1002 has somewhat elevated Ne3O2 ratios at fixed O32 in comparison to both typical high- z and $z \sim 0$ ‘extreme systems. This would suggest the shape of the ionizing radiation field is such that it includes an excess of highly ionizing photons at > 41 eV which is enough for Ne^{++} .

To better gauge the potential of a harder ionizing radiation field, we use Cloudy photoionization modeling and BPASS binary stellar population with age of 1 Myr as the incident radiation field. The electron density is assumed to be $n_e = 800 \text{ cm}^{-3}$ with metallicity of $0.05 Z_\odot$ consistent with EELG1002. We allow for varying measurements of $\log_{10} U$ ranging from -3.5 to -1 in 0.2 dex increments. Our model is overlaid in Figure 7 (green) and we find EELG1002 has Ne3O2 ratio ~ 0.15 dex (5.5σ) above the Cloudy+BPASS prediction at fixed O32. As such, we conclude that EELG1002 most likely has an energetic ISM with a hard ionizing radiation field which could also be enhanced given the combination of low gas-phase metallicity (low metal coolants), high electron temperature, and elevated n_e all resulting in elevated levels of ionizing photons.

4.5. Extreme ξ_{ion} for Low- z ELG but Reminiscent of Typical High- z Galaxies

In previous sections, we find EELG1002 is characterized as having a highly energetic ISM with ionization parameters of $\log_{10} U = -2.23 \pm 0.06$ (Cigale) and $-1.95^{+0.06}_{-0.06}$ (Bagpipes) and a hard ionizing radiation field favoring both O^{++} and Ne^{++} . Measurements of n_e and T_e in conjunction with the ionization parameter, as defined in Equation 7, also show favorable conditions for increased ionizing photon production which, based on our results in §4.2, is attributed to star-formation processes. We report measurements of the ionizing photon production efficiency and 1500 Å magnitudes in Table 6 where we find EELG1002 has $\log_{10} \xi_{ion}^{\text{HII}} = 25.74$ and $M_{UV} = -19.34$ using both Cigale- and Bagpipes-measured continuum. Despite the different IMF and stellar population models assumed in Cigale and Bagpipes, both yield ξ_{ion} are in 1σ agreement consistent

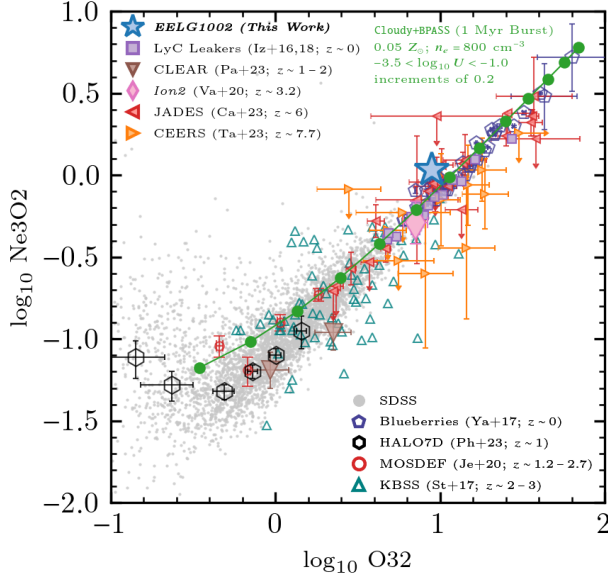


Figure 7. Comparison of Ne3O2 and O32 line ratios as a tracer of harder ionizing radiation spectrum. We find EELG1002 has O32 and Ne3O2 ratios significantly higher than the typical ratios measured by SDSS (Thomas et al. 2013), HALO7D (Pharo et al. 2023), CLEAR (Papovich et al. 2023), MOSDEF (Jeong et al. 2020), and KBSS (Strom et al. 2017). EELG1002 is comparable to known LyC leakers (Izotov et al. 2016, 2018), *Ion2* (Vanzella et al. 2020), and $z > 6$ galaxies (Cameron et al. 2023; Tang et al. 2023). Compared to our Cloudy+BPASS model (green), we find EELG1002 has 0.15 dex higher Ne3O2 at fixed O32 which would suggest a harder ionizing radiation field (e.g., more energetic EUV photons).

with expectations for young, metal-poor stellar populations. However, we note that ξ_{ion} can also be influenced by other factors such as metallicity, IMF, and stellar evolution effects. Both the Cigale and Bagpipes-based ξ_{ion} measurements are well above the canonical value expected of high- z star-forming galaxy populations (e.g., $\xi_{ion} \sim 10^{25.1-25.3} \text{ erg}^{-1} \text{ Hz}$; Robertson et al. 2013). EELG1002 also has elevated ξ_{ion} relative to galaxies in the local Universe and at $z \sim 1$. Local LyC leakers are reported to range between $\xi_{ion} \sim 10^{25.1-25.5} \text{ erg}^{-1} \text{ Hz}$ (Schaerer et al. 2016). Compact star-forming galaxies at $0 < z < 1$ are found to range from $10^{24.5-25.5} \text{ erg}^{-1} \text{ Hz}$ with a small fraction extending up to $10^{25.8} \text{ erg}^{-1} \text{ Hz}$ consistent with EELG1002 (Izotov et al. 2017). We also find EELG1002 has higher ξ_{ion} compared to typical $z \sim 2$ galaxies which report typical $\xi_{ion} \sim 10^{24.8-25.3} \text{ erg}^{-1} \text{ Hz}$ (Matthee et al. 2017; Shivaei et al. 2018).

Figure 8 shows ξ_{ion} of EELG1002 versus [OIII]+H β EW (left panel) where we find it is consistent with the highest known EW emitters identified in CEERS at $5 < z < 8$ (Chen et al. 2024) and $7 < z < 9$ (Tang et al. 2023), as well as past $z \sim 7$ *Spitzer*/IRAC excess studies (Endsley et al. 2021a). The right panel of Figure 8 shows ξ_{ion} ver-

Table 5. Basic morphology properties from pysersic using *HST*/ACS F814W imaging. The effective radius, r_e , and index, n , are based on the best-fit Sérsic profile. Dynamical mass is measured using Equation 10 with uncertainties also factoring in varying scaling factors between 1 – 5 (§3.8).

Property	Measurement
r_e (pc; proper)	529^{+13}_{-14}
n	$1.95^{+0.10}_{-0.09}$
Dynamical Mass ($10^9 M_\odot$)	$4.21^{+27.85}_{-4.20}$

sus sSFR where we use H β SFR along with stellar mass from Cigale and Bagpipes to measure sSFR, as reported in Table 6. We find EELG1002 in both the Cigale and Bagpipes-based measurement has ξ_{ion} and sSFR also consistent with $7 < z < 9$ galaxies identified in CEERS (Whitler et al. 2024) and MIDIS (Rinaldi et al. 2023) and in the *JWST* ERO results (Sun et al. 2023). Both the sSFR and ξ_{ion} of EELG1002 are highly elevated relative to even $z \sim 2$ galaxy populations studied in VANDELS (Castellano et al. 2023). This suggests that EELG1002 is not only highly efficient in producing ionizing photons, but also is efficient at levels highly consistent with even some of the most starburst, high [OIII]+H β EW emitters currently being identified with *JWST* in the $z > 7$ Universe. In this regard, EELG1002 is an interesting case study of the ionizing properties of high- z star-forming galaxies but within the low- z Universe.

4.6. Recent Rapid Burst of Star Formation

The ISM and ionization properties of EELG1002 suggest a stellar population that is dominated by young, massive stars capable of producing large quantities of ionizing photons and a harder ionizing radiation spectrum. This also indicates that EELG1002 is undergoing a recent, rapid increase/burst of star formation activity. As described in §3.5, we explore both parametric (delayed- τ + recent burst; Cigale) and non-parametric (Bagpipes) star formation history modeling in our SED fitting.

Table 6 shows SFRs measured on different timescales where we find that both Cigale and Bagpipes measure about an order-of-magnitude increase in the SFRs from 100 to 10 Myrs. Despite the different modeling used, we find that both parametric and non-parametric SFH models are consistent with 100 Myr SFRs of $\sim 0.2 - 0.4 M_\odot \text{ yr}^{-1}$ and a rapidly increasing SFH reaching 10 Myr SFRs of $\sim 1.7 - 2.5 M_\odot \text{ yr}^{-1}$. Only Cigale measures a 1 Myr SFR of $22.33 \pm 4.35 M_\odot \text{ yr}^{-1}$ as this is the default minimum time resolution in its SFH modeling, while Bagpipes non-parametric SFH has a time resolution of 3 Myr (see §3.5.2) with SFR if $5.39^{+0.22}_{-0.16} M_\odot \text{ yr}^{-1}$. This is relatively consistent with the H β SFR of $7.7 \pm 0.4 M_\odot \text{ yr}^{-1}$ measured using Kennicutt (1998a) calibration assuming Chabrier (2003) IMF which traces timescales of $\sim 1 - 10$ Myr (depending on the

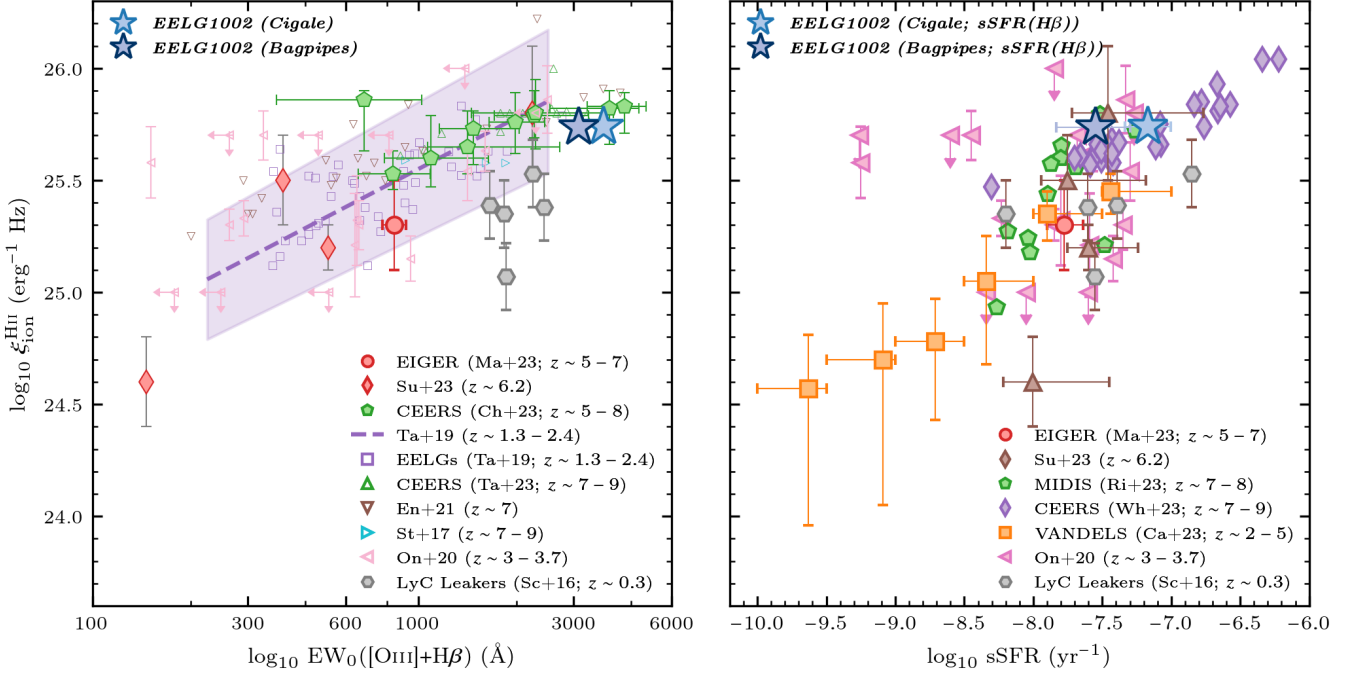


Figure 8. *Left:* Ionizing photon production efficiency, ξ_{ion} , in terms of [OIII]+H β EW. EELG1002 is found to have ξ_{ion} higher than $z \sim 1.3 - 2.4$ EELGs (Tang et al. 2019), $5 < z < 7$ EIGER (Matthee et al. 2023), and $z \sim 6.2$ JWST/ERS (Sun et al. 2023). We find EELG1002 has ξ_{ion} mostly consistent with the highest EW emitters identified at $3 < z < 9$ (Stark et al. 2017; Onodera et al. 2020; Endsley et al. 2021a; Tang et al. 2023; Chen et al. 2024). *Right:* ξ_{ion} in terms of sSFR. EELG1002 is found to be consistent with the highest sSFR and ξ_{ion} sources identified in CEERS (Whitler et al. 2024) and MIDIS (Rinaldi et al. 2023) while also being higher than $2 < z < 5$ galaxies in VANDELS (Castellano et al. 2023) and EIGER. This highlights how EELG1002 has ionization properties consistent with some of the most ‘extreme’, bursty, and ionizing sources currently identified at $z > 5$ and provides a unique case study of low- z analogs of high- z galaxies.

Table 6. Best-Fit Cigale and Bagpipes stellar mass, SFR, and sSFR measurements. Star Formation Rate Surface Density, Σ_{SFR} , is measured using the effective radius from pysersic as shown in Table 5 and defined by Equation 11. SFR from Bagpipes are measured by taking the inferred SFH and integrating on the timescales listed below. Note that the Bagpipes SFR(1 Myr) is constant up to 3 Myr. The SFR measurements for GMOS are based on H β emission and cover a timescale of $\sim 3 - 10$ Myr. The two measurements for GMOS sSFR are based on the H β SFR divided by the Cigale stellar mass and Bagpipes stellar mass in that order. ξ_{ion} is measured using Equation 8 and M_{UV} is measured based on the best-fit SED continuum flux within a $1500 \pm 50 \text{ \AA}$ top-hat filter.

Property	Cigale	Bagpipes	GMOS
Stellar Mass ($10^8 M_{\odot}$)	1.14 ± 0.44	$2.75^{+1.61}_{-1.77}$	—
SFR (1 Myr; $M_{\odot} \text{ yr}^{-1}$)	22.33 ± 4.35	$5.39^{+0.22}_{-0.16}$	$*7.72^{+0.36}_{-0.36}$
SFR (10 Myr; $M_{\odot} \text{ yr}^{-1}$)	2.48 ± 0.12	$1.67^{+0.13}_{-0.10}$	—
SFR (100 Myr; $M_{\odot} \text{ yr}^{-1}$)	0.41 ± 0.11	$0.21^{+0.06}_{-0.04}$	—
Σ_{SFR} (1 Myr; $M_{\odot} \text{ yr}^{-1} \text{ kpc}^{-1}$)	$12.77^{+2.45}_{-2.52}$	$3.08^{+0.19}_{-0.19}$	$*4.39^{+0.29}_{-0.30}$
Σ_{SFR} (10 Myr; $M_{\odot} \text{ yr}^{-1} \text{ kpc}^{-1}$)	$1.41^{+0.11}_{-0.09}$	$0.95^{+0.08}_{-0.08}$	—
Σ_{SFR} (100 Myr; $M_{\odot} \text{ yr}^{-1} \text{ kpc}^{-1}$)	$0.23^{+0.07}_{-0.06}$	$0.12^{+0.03}_{-0.03}$	—
sSFR (1 Myr; Gyr^{-1})	195.65 ± 83.89	$19.63^{+11.50}_{-12.63}$	$(67.64^{+26.02}_{-26.02}, 28.10^{+16.47}_{-18.11})$
sSFR (10 Myr; Gyr^{-1})	21.73 ± 8.37	$6.08^{+3.58}_{-3.92}$	—
sSFR (100 Myr; Gyr^{-1})	3.57 ± 1.68	$0.76^{+0.49}_{-0.51}$	—
ξ_{ion}^{HII} ($\text{erg}^{-1} \text{ Hz}$)	$25.74^{+0.03}_{-0.03}$	$25.74^{+0.02}_{-0.02}$	—
M_{UV} (mag)	$-19.33^{+0.06}_{-0.06}$	$-19.34^{+0.03}_{-0.03}$	—
$EW_0([OIII] + H\beta)$ (\AA)	$3697.80^{+29.53}_{-29.73}$	$3101.15^{+25.00}_{-25.15}$	—

stellar population model). Overall, the SFRs suggest an intense, rapidly increasing burst of star-formation activity in recent times.

For a low-mass galaxy such as EELG1002, a high SFR would be indicative of high specific SFR (sSFR) placing it well above the SFR – stellar mass correlation (‘starburst’; e.g., Speagle et al. 2014). Table 6 includes the sSFR measured on 1, 10, and 100 Myr timescales along with H β -measured sSFR assuming both the stellar mass measured from Cigale and Bagpipes. As we saw for the SFRs, the sSFR also increases an order-of-magnitude from 100 to 10 Myr as well as from 10 to 1 Myr. We also find H β -measured sSFR of $67.5 \pm 26 \text{ Gyr}^{-1}$ (Cigale) and $28.1^{+16}_{-18} \text{ Gyr}^{-1}$ (Bagpipes) which would mean mass doubling times (inverse of the sSFR) $\sim 15 - 35 \text{ Myr}$. This suggests that not only is EELG1002 undergoing a rapid burst of star formation activity, but is also rapidly building up its stellar mass content.

Star Formation Rate Surface Densities, Σ_{SFR} are measured as:

$$\Sigma_{\text{SFR}} = \frac{\text{SFR}}{2\pi r_e^2} \quad (11)$$

and are shown in Table 6. Given the compact nature of EELG1002 along with its high SFR, we find that Σ_{SFR} on short timescales is quite high reaching $\sim 12.7 \text{ M}_{\odot} \text{ yr}^{-1} \text{ kpc}^{-2}$ in the instantaneous, 1 Myr SFR measured with Cigale. The H β -measured Σ_{SFR} is somewhat lower at $4.4 \pm 0.3 \text{ M}_{\odot} \text{ yr}^{-1} \text{ kpc}^{-2}$ and in better agreement with $3.1 \pm 0.2 \text{ M}_{\odot} \text{ yr}^{-1} \text{ kpc}^{-2}$ measured with Bagpipes. However, all our measurements of Σ_{SFR} are similar to galaxies with similar O32, stellar mass, and U at $z > 3$ (Reddy et al. 2023). This suggests that star formation activity is quite compact in EELG1002 and may be another reason why properties such as ξ_{ion} , T_e , and U are elevated given the concentration of recently formed hot, massive stars collectively releasing ionizing photons into the ISM.

5. DISCUSSION

5.1. Realistic Star Formation Histories or Outshining Effect?

The rapidly rising and intense star-formation history of EELG1002 without any past star-formation activity at higher lookback times does raise the question: *does the star formation histories conform to our current framework of galaxy formation & evolution or is this a result of an outshining effect?* The latter would suggest that the recently formed young stellar population is bright enough to ‘outshine’ the old, mature stellar population formed at older lookback times. This would result in a biased SFH and an underestimation in stellar masses (Narayanan et al. 2024). In the case of EELG1002, we have near-IR constraints from CFHT/WIRCam and *HST* WFC3/F140W to potentially con-

strain the older stellar population. Future IR observations (e.g., $> 1 \mu\text{m}$ rest-frame) could provide better constraints on the old stellar population, if present.

However, *does such SFHs even fit within the framework of galaxy formation & evolution?* To answer this question, we look at the Illustris simulation (Genel et al. 2014; Vogelsberger et al. 2014a,b; Nelson et al. 2015) for analogs of EELG1002. We search for analogs within TNG50, 100, and 300 in snapshot #55 ($z = 0.82$) that have properties broadly consistent with EELG1002: $\text{SFR} > 3 \text{ M}_{\odot} \text{ yr}^{-1}$, stellar mass between 10^7 and $10^{8.7}$, and *ugriz* magnitudes near -19.5 ± 1 mag. We also limit the analogs to those that have not undergone a recent merger with another subhalo and also have gas-phase metallicities roughly consistent with EELG1002.

In total, we identify 2 strong candidates within TNG300-2 in snapshot #55 with IDs of 182200 and 119294 and show the star-formation histories in Figure 9. In the case of 182200, the subhalo was recently formed with a rapid increase in its star formation rates. This does not necessarily mean that such a galaxy has formation time at $z \sim 0.8$ rather the subhalo and all associated particles were resolved by this snapshot in the simulation. The SFR measured at the first snapshot (#53; $z \sim 0.89$) was $0.04 \text{ M}_{\odot} \text{ yr}^{-1}$ and quickly rose by almost two orders of magnitude to $3.1 \text{ M}_{\odot} \text{ yr}^{-1}$ by $z \sim 0.82$ all within a $\sim 330 \text{ Myr}$ time frame. This is very much reminiscent of the rapid and intense burst of star-formation we find based on both parametric and non-parametric SFH modeling of EELG1002.

On the other hand, 119294 is somewhat older with a resolved formation time extending back to $z \sim 1.1$ where it starts with a small initial burst of $\sim 0.26 \text{ M}_{\odot} \text{ yr}^{-1}$ that quickly died out within $\sim 250 \text{ Myr}$ and remained inactive with no star-formation activity until $z \sim 0.89$. At this point, 119294 had a star formation rate of $0.06 \text{ M}_{\odot} \text{ yr}^{-1}$ and rapidly increased in SFR up to $3.9 \text{ M}_{\odot} \text{ yr}^{-1}$ by $z \sim 0.82$ very much similar to 182200. Overall, this suggests that the SFH we find for EELG1002 does conform with our current framework for galaxy formation & evolution. Our comparison to Illustris analogs also suggests that EELG1002 may have undergone previous minor bursts of star-formation as well which could form a low-mass older population. Deep near-IR imaging and spectroscopy could shed light if such a population exists; however, based on the available evidence, EELG1002 has an SFH described as a rapid burst within a $\sim 10 \text{ Myr}$ timescale that is found to be ‘realistic’ in this regard that EELG1002-like sources do show within large-scale cosmological simulations such as Illustris.

5.2. What is driving the intense star formation activity?

Given that such intense star formation activity is supported by simulations, a follow-up question that arises is: *what is driving such intense, rapid star formation activity?* In order

to have such star formation requires that a galaxy has a substantial amount of cold gas available and a pathway for the accretion of more cold gas to continuously refuel the reservoir. In the case of EELG1002, we find mass doubling times of $\sim 15 - 35$ Myr that would suggest a sizable amount of cold gas is available to cause such rapid stellar mass growth. The low gas-phase metallicity of EELG1002 would also suggest that cold and relatively untouched gas reservoirs are available and that, as we saw in the Illustris analogs, EELG1002 may be undergoing a first starburst phase. Otherwise, given its redshift, we would expect a higher gas-phase metallicity reflecting chemical enrichment from past star formation episodes.

The *middle* panel of Figure 9 also supports the idea that gas fractions within sources like EELG1002 are quite elevated. In the two Illustris analogs, we find gas masses of $\sim 10^9 M_\odot$ which is $10 - 100 \times$ higher than its stellar mass content corresponding to $> 90\%$ gas fractions. The low gas metallicities in the analogs shown in the *bottom* panel of Figure 9 demonstrate the lack of chemical evolution given very little past star formation activity at earlier times.

Observationally, we find evidence for potentially high gas fractions within EELG1002. The dynamical mass of EELG1002 is $\sim (4.2^{+27.9}_{-4.2}) \times 10^9 M_\odot$ and represents the combination of stellar, gas, and dark matter within the galaxy. Although dynamical mass also includes the dust mass, we find based on Balmer Decrement that $E(B-V) \sim 0$ mag such that dust mass is most likely negligible. The dynamical mass relative to the stellar mass based on Cigale and Bagpipes suggests that $> 90\%$ of the dynamical mass consists of both gas and dark matter consistent with the Illustris analogs suggesting a high gas fraction. Inversing the Kennicutt-Schmidt law (Kennicutt 1998b) and using the Σ_{SFR} measurement based on H β emission (see Table 6), we find an inferred gas mass of $\sim 10^9 M_\odot$ comparable to the dynamical mass. Sources at similar [OIII] luminosity as EELG1002 are also found to reside in halos with typical masses ranging between $\sim 10^{12.5}$ and $10^{13} M_\odot$ (Khostovan et al. 2018) which would suggest for deep gravitational potentials that would facilitate the inflow of gas. The Illustris analogs also reside in group halos with dark matter mass of $\sim 10^{12.2}$ and $10^{12.6} M_\odot$ for 182200 and 119294, respectively. Although we do not observe any gas inflow features based on the GMOS spectra, enhanced pristine cold gas accretion mixing with the ISM could also reduce the gas-phase metallicity.

We conclude that the SFH of EELG1002 is not due to an outshining effect and that it conforms to our current framework of galaxy formation and evolution as seen by the Illustris analogs. EELG1002 is most likely undergoing a first bursty phase of star formation activity as expected in high- z galaxies (e.g., Cohn et al. 2018) which can also explain the high [OIII] EW given the lack of past stellar mass growth

(low continuum flux density). What is most likely driving the intense star formation activity is the availability of copious amounts of gas (high gas fractions) coupled with potentially residing in dark matter halos with masses sufficient to facilitate the inflow of cold gas to replenish the gas reservoirs. Inversing the Kennicutt-Schmidt law (Kennicutt 1998b) and measuring the gas-consumption timescale such sustained star formation can persist for ~ 250 Myr comparable to what is found for the Illustris analogs. Follow-up observations with ALMA could shed light on the amount of cold, molecular gas available within EELG1002, as well as how efficiently the gas is being converted into stars (e.g., star formation efficiency).

5.3. What becomes of sources like EELG1002?

Studies suggest that compact star-forming galaxies are the progenitors of compact, massive quiescent galaxies (Barro et al. 2013; Zolotov et al. 2015). We use the analogs identified in Illustris to map out the evolutionary path of EELG1002-like sources. Figure 9 shows the SFH (*top*), gas and stellar mass growth (*middle*), and gas and stellar chemical enrichment histories (*bottom*). In both analogs, we find that the recent rise in star formation activity is part of an increasingly intense period of star formation. We will discuss the evolutionary path of each analog separately below with 119294 and 182200 shown in *green* and *red* in Figure 9.

119294: This analog starts with a small, minor burst of star formation (*top* panel inset of Figure 9) at $z \sim 1.1$ (particle resolution limit in Illustris; not necessarily t_{form}) that dies out within ~ 300 Myr. This is followed by a single, large burst in star-formation activity starting at $z \sim 0.8$ that was sustained for 1 Gyr before eventually coming to a halt by $z \sim 0.5$ and lacking any significant star-formation activity down to $z \sim 0$. The system contained a high gas-to-stellar mass ratio at $z > 0.8$ that fueled the rapidly increasing SFH. By the next snapshot (~ 100 Myr), 119294 nearly tripled its stellar mass from 2 to $5.5 \times 10^8 M_\odot$ and maintained a gas mass of $\sim 10^{10} M_\odot$. By $z = 0.73$ (~ 500 Myr later), 119294 experienced a merging event with a massive system which explains the rapid rise in SFH that persisted up to $z \sim 0.7$ followed by a decrease and eventual halt in star formation activity. The chemical enrichment of 119294 during the pre-merge star formation activity also shows gas metallicities doubling from 0.128 to $0.205 Z_\odot$ and stellar metallicities from 0.111 to $0.152 Z_\odot$ highlighting a rapid chemical enrichment period within 100 Myrs. After the merger event, we find 119294 eventually becomes an essentially ‘dead’/quiescent massive galaxy ($\sim 10^{10} M_\odot$) with very little gas mass and chemical enrichment consistent with $\sim Z_\odot$.

182200: The *top* panel of Figure 9 shows a rapid increase in star formation activity starting at $z \sim 0.85$ (7.2 Gyr ago) where by $z \sim 0.82$ the SFR reaches $\sim 3 M_\odot \text{ yr}^{-1}$ with stellar

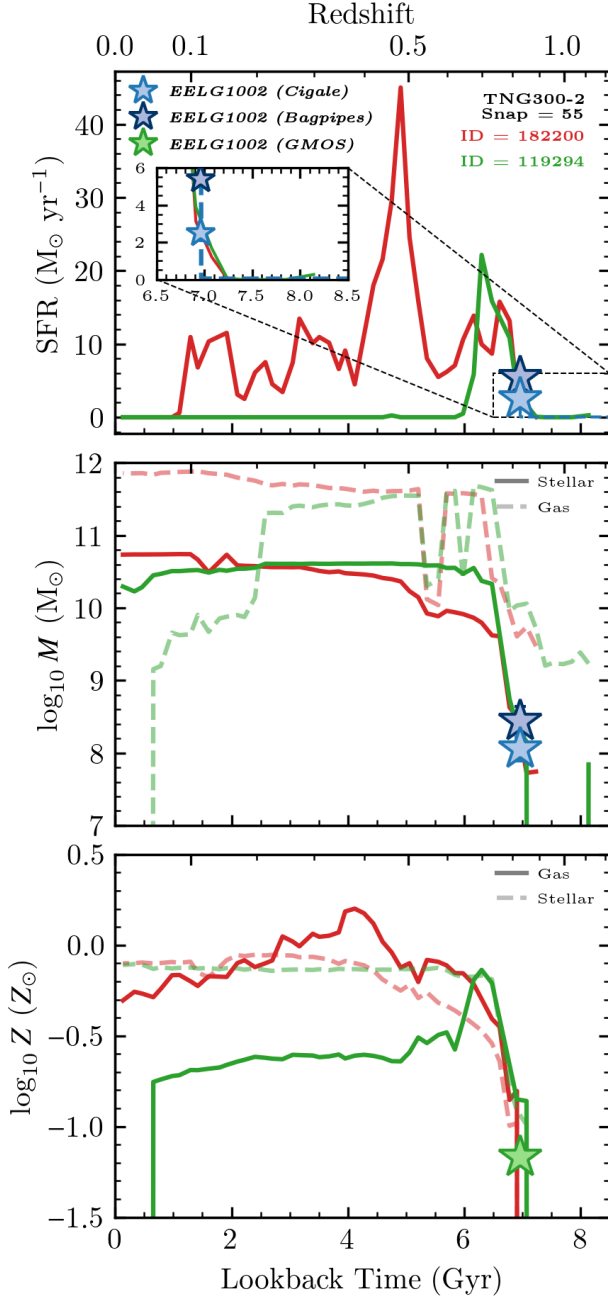


Figure 9. Illustris Analogs of EELG1002 with their respective star formation (*top*), stellar and gas mass (*middle*), and chemical enrichment (*bottom*) histories. Both analogs show a rapid increase in star formation activity occurring at $z \sim 0.8$ signifying a first starburst phase where both are chemically unevolved and supported by high gas masses. Rapid chemical enrichment and stellar mass buildup occur within 100 – 250 Myrs. Subsequent histories past $z < 0.7$ are different between both analogs owing to various mergers; however, both eventually become $10^{10-11} M_{\odot}$ galaxies with solar-level metallicities. Therefore, EELG1002-like sources may potentially merge with more massive systems to become large structures in the local Universe. However, if EELG1002 remains isolated, then it could be the progenitor of a massive, compact quiescent galaxy (e.g., Barro et al. 2013; Zolotov et al. 2015).

mass of $3.2 \times 10^8 M_{\odot}$ and gas mass of $4 \times 10^9 M_{\odot}$, highlighting the gas-enriched environment that fuels the star formation activity. By the next snapshot (100 Myr later), the SFR increases to $13.2 M_{\odot} \text{ yr}^{-1}$ with a stellar mass of $4.2 \times 10^8 M_{\odot}$ and gas mass of $8.8 \times 10^9 M_{\odot}$, where the increase in gas mass indicates accretion to replenish the gas reservoir. 182200 experiences its first merging event by $z \sim 0.75$ followed by subsequent merging events corresponding to the peaks in its SFH (*top* panel of Figure 9) and by $z \sim 0.1$ eventually halts in star formation activity. The gas mass remains quite high by $z \sim 0$ and could indicate hot gas remains within this system. The chemical enrichment history pre-first merger shows a rapid increase within ~ 250 Myr from $0.04 Z_{\odot}$ ($z \sim 0.85$) to $0.14 Z_{\odot}$ ($z \sim 0.8$). After the merging events, we find 182200 shows an increase to $\sim Z_{\odot}$ within 1 – 1.5 Gyr after the initial burst. We find a similar chemical enrichment history when looking at stellar metallicities. By $z \sim 0$, 182200 has evolved into a chemically mature quiescent galaxy with stellar masses of a few times $10^{10} M_{\odot}$.

Based on these two analogs alone, we find EELG1002 could most likely experience a merging event somewhere along its 7 Gyr history to the present-day and coalesce to become the massive, chemically-enriched galaxies that we see today. However, in the case that EELG1002 remains isolated (e.g., ‘field galaxy’), then it could potentially evolve in isolation into a massive, compact quiescent galaxy (e.g., Barro et al. 2013; Zolotov et al. 2015).

5.4. Lack of HeII4686Å: Upper Limit in Ionizing Spectrum or Too Weak?

As we show in §4.4, the ISM of EELG1002 is quite energetic and we find evidence for a hard ionizing radiation field given an elevated Ne3O2 ratio compared to O32. This suggests conditions for which Ne^{++} is easily produced (requires 41 eV) compared to O^{++} (requires 35 eV). Coupled with the high $\text{H}\beta$ EWs (signature of young stellar populations; e.g., Fernandes et al. 2003; Levesque & Leitherer 2013), we would expect very high ionization potential lines such as He^{++} which requires 54 eV. Past studies also suggest that galaxies having undergone a recent star-formation event and are dominated by low-metallicity young populations with high ionizing conditions are capable of producing HeII emission (e.g., Schaerer 2003; Saxena et al. 2020; Berg et al. 2021). Observations also suggest a potential increase in HeII4686Å emission with decreasing gas-phase metallicities at $12 + \log_{10}(\text{O}/\text{H}) < 8$ (Senchyna et al. 2019).

Despite the conditions favoring HeII emission within EELG1002, we find no evidence of HeII4686Å emission in the GMOS spectra (*top* panel of Figure 2). Although a lack of such emission could be an indication that there is an upper limit in the ionizing spectrum associated with EELG1002, we explore the possibility HeII4686Å emission

was too faint to be observed with the GMOS observations (exposure time of 3600 seconds). HeII4686Å is included in the Cloudy models that were used within Bagpipes where we find that HeII is predicted to have a line flux of $\sim 2 \times 10^{-19}$ erg s $^{-1}$ cm $^{-2}$ which does place it well below the detection limit ($\sim 9.4 \times 10^{-18}$ erg s $^{-1}$ cm $^{-2}$ about 4686 ± 20 Å at 3σ). However, studies have shown that photoionization models underestimate the contribution of HeII emission (e.g., Nanayakkara et al. 2019; Berg et al. 2021). Senchyna et al. (2019) investigate the HeII4686Å/H β line ratio as a function of $12 + \log_{10}(\text{O}/\text{H})$ for a sample of six $z < 0.01$ extremely metal-poor ($Z < 0.1 Z_{\odot}$) galaxies and reported a gradient where HeII emission was found to increase with decreasing gas-phase metallicity. Using their empirical measurement, we expect HeII4686Å/H β in the range of ~ 0.01 to 0.04 at $12 + \log_{10}(\text{O}/\text{H}) \sim 7.5$ which would correspond to an HeII4686Å line flux of $\sim 1.87 - 7.48 \times 10^{-18}$ erg s $^{-1}$ cm $^{-2}$ which is still well below our detection limit at the 3σ level. This would suggest that EELG1002 may have an ionizing spectrum that does extend to ionizing energies capable of producing He $^{++}$; however, our current data is not sensitive to such line fluxes to observe HeII 4686Å.

Overall, the lack of HeII4686Å does not necessarily suggest an upper limit in the ionizing spectrum but more likely that the GMOS data was not sensitive to observe this specific HeII line. However, this does raise the prospect of observing HeII1640Å which is typically $6 - 8 \times$ brighter than the 4686Å line (based on PyNeb getEmissivity for He). Indeed if HeII1640Å is observed within EELG1002, it would suggest very high ionizing conditions that are reminiscent of galaxies in the early Universe. Especially given that we find no evidence for X-ray binaries given the lack of X-ray detections (see §4.2) and presence of Wolf-Rayet stars (lack of a blue WR bump; e.g., Guseva et al. 2000), then the main source could potentially be from a young, low-metallicity stellar population (Saxena et al. 2020). Observations with HST/COS are needed to observe HeII1640Å to confirm this.

5.5. Conditions for LyC Escape

EELG1002 potentially has conditions that could facilitate LyC escape. The compact size and Σ_{SFR} in conjunction with the elevated U and ξ_{ion} suggest large quantities of ionizing photons are available and concentrated. This is also backed by the recent SFR, sSFR, and H β EW $\sim 404 - 473$ Å suggesting the presence of a largely young stellar population is present within EELG1002. Mechanical feedback mechanisms such as stellar-driven or SNe-driven winds could result in the creation of low HI column density channels allowing for Ly α and LyC escape (e.g., Yang et al. 2016; Pucha et al. 2022; Reddy et al. 2022). Such outflows are not seen within the GMOS spectra (e.g., asymmetric line profiles) but may be observable within rest-frame UV spectroscopy

via P Cygni profiles around high ionization lines. Available GALEX/FUV photometry also suggests a non-zero LyC escape fraction (f_{esc}) with measured $\text{mag}_{\text{AUTO}} = 26.25 \pm 0.34$ ($\sim 3\sigma$ detection). However, the GALEX/FUV photometry could be contaminated by light redwards of the Lyman limit and suffer from blending issues due to the poor spatial resolution of GALEX and the close angular proximity of two sources (see Figure 1). Without spatially-resolved UV imaging and/or deep UV spectroscopy, we can not directly measure f_{esc} for EELG1002 although the conditions would suggest that LyC escape is present.

Past studies have developed empirical calibrations to estimate f_{esc} given observables. We use these indicators to infer f_{esc} but note that various caveats are associated with each calibration for which we refer the reader to Choustikov et al. (2024) for a detailed overview. We first use the empirical O32 calibration of Faisst (2016) and infer $f_{\text{esc}} > 0.115$ at the 90% confidence level. We next use the UV spectral slope, β , calibration of Chisholm et al. (2022) which was based on sources observed in the Low- z Lyman Continuum Survey (LzLCS). In both Cigale and Bagpipes SED fitting, we find EELG1002 has $\beta \sim -2.5$ and corresponds to $f_{\text{esc}} \sim 0.08 - 0.21$ based on this calibration. Next, we use the Σ_{SFR} calibration of Naidu et al. (2020) motivated by more compact, star-forming systems with high Σ_{SFR} having higher f_{esc} given feedback mechanisms forming low-density channels allowing for LyC escape. We infer $f_{\text{esc}} \sim 0.15 - 0.22$ using this calibration. Lastly, Choustikov et al. (2024) developed a combined f_{esc} indicator that is dependent on several key properties related to LyC escape: β , $E(B - V)$, H β luminosity, M_{UV} , $R23$, and O32. We find an inferred $f_{\text{esc}} \sim 0.13$ using this calibration. Overall, EELG1002 potentially has $f_{\text{esc}} \sim 0.1 - 0.2$ based on the above mentioned calibrations and future rest-frame UV observations are needed for confirmation.

5.6. Ideal Case of Reionization-Era Galaxies?

EELG1002 is a uniquely extreme source at $z \sim 0.8$ but may represent the conditions that existed in Reionization-era galaxies. Throughout this paper, we have noted how EELG1002 is similar to galaxies currently being observed in the $z > 5$ Universe by JWST. We found that EELG1002 has [OIII]+H β EW at fixed stellar mass even higher than typical star-forming galaxies observed in EIGER (Matthee et al. 2023) and JADES (Boyett et al. 2024). Gas-phase metallicity, ionization parameter, and excitation state ($R23$) are also found to be similar to $z > 5$ galaxies. ξ_{ion} at fixed [OIII]+H β is highly consistent with $z \sim 7 - 9$ galaxies from CEERS (Tang et al. 2023). EELG1002 also has sSFR and ξ_{ion} consistent with some of the most extreme systems identified in CEERS (Whitler et al. 2024) and MIDIS (Rinaldi et al. 2023). The optical size of EELG1002 is ~ 530 pc and is

consistent with the typical optical sizes of $7 < z < 9$ galaxies at similar 4800\AA rest-frame magnitudes (-18.8 mag; ~ 400 pc with scatter up to ~ 700 pc; Yang et al. 2022b). Overall, EELG1002 matches with $z > 5$ galaxies in many ways which highlights a key point that this system represents similar characteristics and properties as galaxies within the Epoch of Reionization. Future follow-up studies of EELG1002 can shed more light on the ionization and star formation processes in the context of what may have also occurred at high- z . Although EELG1002 is only a single object, the work presented here motivates for similar searches of high EW objects within archival datasets which can form statistically larger samples of low- z ‘extreme’ galaxies similar to typical star-forming galaxies observed at $z > 5$ and used to study Reionization Era-like galaxies in great detail.

6. CONCLUSIONS

In this paper, we have presented a detailed analysis of a $z = 0.8275$ extreme emission line galaxy, EELG1002, which was identified as part of ongoing work of the COSMOS spectroscopic archive within 7 year old Gemini GMOS-S spectroscopic data. We use all available spectroscopic and photometric data to investigate the nature of this source in great detail. Our main results are:

- (i) EELG1002 has rest-frame $[\text{OIII}]+\text{H}\beta$ EW ~ 3100 to 3700\AA with stellar mass of $\sim 10^8 M_\odot$ depending on the SED fitting model assumed for the continuum flux density. This is found to be $\sim 32 - 36\times$ higher than the typical $[\text{OIII}]+\text{H}\beta$ EW for $z \sim 0.8$ at similar stellar mass outlining the extremity and rarity of such a source. The $[\text{OIII}]+\text{H}\beta$ EW is also higher than typical $z > 3$ ELGs (Khostovan et al. 2016; Boyett et al. 2024) and even $z \sim 5 - 7$ galaxies (Matthee et al. 2023) and comparable to known local LyC leakers.
- (ii) Strong $\text{H}\beta$ emission suggests recent star formation rates of $7.7 M_\odot \text{ yr}^{-1}$ with mass doubling timescales of $\sim 15 - 35$ Myr. Combined with its compact size ($r_{\text{eff}} \sim 530$ pc; proper), we find EELG1002 has $\Sigma_{\text{SFR}} \sim 4.4 M_\odot \text{ yr}^{-1} \text{ kpc}^{-2}$. Star formation history modeling using spectrophotometric SED fitting (Cigale and Bagpipes) also confirms the bursty star-forming nature of EELG1002 with no past star-formation activity at older lookback times.
- (iii) We find no clear evidence of an AGN component in EELG1002 given the lack of broad emission line features, X-ray detection, and the necessary $[\text{OIII}]/\text{H}\beta$ and stellar mass to fall within the AGN classification using MEx diagnostic. $[\text{OIII}]/\text{H}\beta$ ratio coupled with low metallicity from direct T_e would suggest low $[\text{NII}]/\text{H}\alpha$ making EELG1002 also fall within the BPT star-forming classification. There may be a potential obscured AGN component given *Spitzer*/IRAC pho-

tometry; however, it is blended with 2 nearby sources. Furthermore, a dust obscured AGN may be unlikely given that Balmer Decrements suggest $E(B - V) = 0$ mag.

- (iv) We find EELG1002 is metal poor with $12 + \log_{10}(\text{O}/\text{H}) = 7.52 \pm 0.07$ ($Z_{\text{gas}} = 0.068^{+0.013}_{-0.009} Z_\odot$) based on direct T_e measurements using the auroral $[\text{OIII}]\lambda 4363\text{\AA}$ line. At the measured stellar mass, we find EELG1002 has gas-phase metallicity consistent with $z > 5$ galaxies. Other known low- z analogs of high- z galaxies show higher stellar mass and metallicity compared to EELG1002 which would suggest some past star-formation activity and chemical enrichment. However, the low metallicity and stellar mass of EELG1002 suggests a lack of chemical evolution and past star-formation activity such that EELG1002 may represent a galaxy undergoing a potential first bursty phase of star formation.
- (v) Spectrophotometric SED fitting using both Cigale and Bagpipes show elevated ionization parameters with $\log_{10} U \sim -2.23$ and -1.96 , respectively. $[\text{OIII}]/[\text{OII}]$ ratios also suggest highly energetic ISM conditions and elevated $[\text{NeIII}]/[\text{OII}]$ at fixed $[\text{OIII}]/[\text{OII}]$ show evidence of a harder ionizing radiation field (e.g., more EUV photons). The lack of $\text{HeII}\lambda 4686\text{\AA}$ emission is due to the observations not going deep enough to detect the line rather than an upper limit in the ionizing spectrum at 54 eV. Deep rest-frame UV spectroscopic follow-up could potentially yield $\text{HeII}\lambda 1640\text{\AA}$ which is typically $\sim 6 - 8\times$ brighter than its 4686\AA counterpart.
- (vi) EELG1002 has $\log_{10} \xi_{\text{ion}} \sim 25.74$ that is consistent with some of the most extreme and bursty star-forming galaxies observed at $z > 7$ based on $[\text{OIII}]+\text{H}\beta$ EW and sSFR. The elevated efficiency in producing ionizing photons within EELG1002 may be attributed to a combination of elevated SFR, compact size, low metallicity, and highly energetic ISM condition with evidence of a harder ionizing radiation field.
- (vii) Although we find a 3σ detection within *GALEX*/FUV that would suggest LyC escape, we note that the *GALEX* spatial resolution is poor and the 3σ detection may be contaminated by 2 nearby sources. Using multiple empirical calibrations, we find that EELG1002 may have $\sim 10 - 20\%$ LyC escape fraction.
- (viii) Both parameteric and non-parametric SFH modeling of EELG1002 suggest for a recent burst of star formation with no past activity at older lookback times. Analogs identified in Illustris-TNG suggest such SFHs fall within our current framework of galaxy formation & evolution where intense star formation occurs followed by rapid chemical enrichment and stellar mass

buildup. This is supported by high gas masses in the simulations. Observationally, we find EELG1002 has dynamical mass of $\sim 10^9 M_\odot$ which is an order-of-magnitude higher than its stellar mass suggesting high gas masses similar to what is found in the Illustris analogs.

EELG1002 provides for an interesting and unique case of a low- z galaxy with properties highly consistent with even some of the extreme star-forming galaxies currently being observed at $z > 5$ with *JWST*. The [OIII]+H β EW alone for EELG1002 is record-breaking for a star-forming galaxy at its redshift and stellar mass highlighting not only the extremity but rarity of this source. More importantly, we have demonstrated how such a source at low- z can be used to uncover details on the ionizing and star-formation properties & processes expected to occur in the high- z Universe by using all available evidence and referring to large hydrodynamical simulations for support. This work also emphasizes the importance of archival datasets that are currently being processed and analyzed as part of on-going work in developing the COSMOS Spectroscopic Archive where unpublished data can present surprising scientific discoveries such as EELG1002. Future next-generation surveys planned with *Euclid* and *Roman* will find many EELG1002-like systems given the wide areal coverage resulting in large comoving volumes needed given the rarity (e.g., low number densities) of such sources.

ACKNOWLEDGEMENTS

We thank the anonymous reviewer for their feedback and suggestions that enhanced the quality of this work. AAK thanks Yuichi Harikane, Erini Lambrides, Brian Lemaux, Keunho Kim, Jed McKinney, Mainak Singha, and Ryan

Sanders for useful discussions. AAK also thanks all participants of the NOIRLab First Gigayear(s) Conference at Hilo, Hawaii and the STScI Spring Symposium 2024: “Recipes to Regulate Star Formation at All Scales: From the Nearby Universe to the First Galaxies” for productive comments, feedback, and discussions.

This material is based upon work supported by the National Science Foundation under Grant No. 2009572.

Based on observations obtained at the international Gemini Observatory, a program of NSF NOIRLab, which is managed by the Association of Universities for Research in Astronomy (AURA) under a cooperative agreement with the U.S. National Science Foundation on behalf of the Gemini Observatory partnership: the U.S. National Science Foundation (United States), National Research Council (Canada), Agencia Nacional de Investigación y Desarrollo (Chile), Ministerio de Ciencia, Tecnología e Innovación (Argentina), Ministério da Ciência, Tecnologia, Inovações e Comunicações (Brazil), and Korea Astronomy and Space Science Institute (Republic of Korea).

Software: *astropy* (Astropy Collaboration et al. 2013, 2018, 2022), *numpy* (Harris et al. 2020), *PyQSOFit* (Guo et al. 2018; Shen et al. 2019), *PyNeb* (Luridiana et al. 2015), *pysersic* (Pasha & Miller 2023), *PyPeit* (Prochaska et al. 2020a,b), *Cigale* (Boquien et al. 2019; Yang et al. 2022a), *Bagpipes* (Carnall et al. 2018)

DATA AVAILABILITY

All raw data is publicly available and can be found within the Gemini Science Archive by searching for GS-2017A-FT-9 under Program ID. The associated pypeit reduction files can be found at [GitHub repository](#) and are available for public use.

APPENDIX

REFERENCES

- Amorín, R., Sommariva, V., Castellano, M., et al. 2014a, *A&A*, 568, L8, doi: [10.1051/0004-6361/201423816](#)
- Amorín, R., Grazian, A., Castellano, M., et al. 2014b, *ApJL*, 788, L4, doi: [10.1088/2041-8205/788/1/L4](#)
- Amorín, R., Pérez-Montero, E., Contini, T., et al. 2015, *A&A*, 578, A105, doi: [10.1051/0004-6361/201322786](#)
- Andrews, B. H., & Martini, P. 2013, *ApJ*, 765, 140, doi: [10.1088/0004-637X/765/2/140](#)
- Asplund, M., Amarsi, A. M., & Grevesse, N. 2021, *A&A*, 653, A141, doi: [10.1051/0004-6361/202140445](#)
- Astropy Collaboration, Robitaille, T. P., Tollerud, E. J., et al. 2013, *A&A*, 558, A33, doi: [10.1051/0004-6361/201322068](#)
- Astropy Collaboration, Price-Whelan, A. M., Sipőcz, B. M., et al. 2018, *AJ*, 156, 123, doi: [10.3847/1538-3881/aabc4f](#)
- Astropy Collaboration, Price-Whelan, A. M., Lim, P. L., et al. 2022, *ApJ*, 935, 167, doi: [10.3847/1538-4357/ac7c74](#)
- Atek, H., Furtak, L. J., Oesch, P., et al. 2022, *MNRAS*, 511, 4464, doi: [10.1093/mnras/stac360](#)
- Atek, H., Siana, B., Scarlata, C., et al. 2011, *ApJ*, 743, 121, doi: [10.1088/0004-637X/743/2/121](#)
- Atek, H., Kneib, J.-P., Pacifici, C., et al. 2014, *ApJ*, 789, 96, doi: [10.1088/0004-637X/789/2/96](#)
- Baldwin, J. A., Phillips, M. M., & Terlevich, R. 1981, *PASP*, 93, 5, doi: [10.1086/130766](#)

Table 7. Cigale parameters used in the SED fitting process

Parameter	Symbol	Value
Delayed Exponential Star Formation History with Burst		
e -folding time of the main stellar population model (Gyr)	τ_{main}	0.05, 0.1, 0.25, 0.5, 0.75, 1.0, 2.5, 5.0, 7.5
Age of the main stellar population in the galaxy (Gyr)	t_{main}	0.05, 0.1, 0.25, 0.5, 0.75, 1.0, 2.5, 5.0, 6.6
e -folding time of the late starburst population model (Myr)	τ_{burst}	1, 5, 10, 50, 100
Age of the late burst (Myr)	t_{burst}	1, 5, 10, 25, 50
Mass fraction of the late burst population	f_{burst}	Uniform(0,1) steps of 0.1
Stellar Population Synthesis Model (Bruzual & Charlot 2003)		
Initial mass function	IMF	Chabrier (2003)
Stellar Metallicity (Z_{\odot})	Z_{\star}	0.005, 0.02, 0.2, 0.4, 1.
Nebular Emission Line Spectrum (Cloudy v13.01; Ferland et al. 1998, 2013)		
Ionisation parameter	$\log_{10} U$	Uniform(-3,-1) steps of 0.1
Gas Metallicity (Z_{\odot})	Z_g	0.05 (fixed)
Electron Density (cm^{-3})	n_e	1000
Fraction of Lyman Continuum photons escaping the galaxy	f_{esc}	0.0
Fraction of Lyman Continuum photons absorbed by dust	$f_{\text{esc,dust}}$	0.0
Emission Line Widths (km s^{-1})	Δv_{lines}	400 (fixed)
Dust Attenuation Model (Calzetti et al. 2000)		
Reddening of the nebular lines light for young & old population (mag)	$E(B - V)_I$	0.0 (fixed)
Ratio of $E(B - V)_I$ to Stellar Continuum Reddening (mag)	$f_{E(B-V)}$	1.0 (fixed)
Central wavelength of the UV bump (\AA)	$\lambda_{UV,b}$	2175 (fixed)
Width (FWHM) of the UV bump (\AA)	$\Delta\lambda_{UV,b}$	350
Amplitude of the UV bump (3: Milky Way)	$I_{UV,b}$	0
Slope delta of the power law modifying the attenuation curve	–	0.0
Extinction law to use for attenuating the emission lines flux	–	SMC (Pei 1992)
Total-to-selective extinction ratio for extinction curve applied to emission lines	$A_V/E(B - V)$	2.93
Dust Emission Model (Draine et al. 2014)		
Mass fraction of PAH	q_{PAH}	2.50
Minimum Radiation Field	U_{min}	1.0
Power law slope $dU/dM \propto U^{\alpha}$	α	2.0
Fraction illuminated from U_{min} to U_{max}	γ	0.1

1570 Barro, G., Faber, S. M., Pérez-González, P. G., et al. 2013, ApJ,
1571 765, 104, doi: [10.1088/0004-637X/765/2/104](https://doi.org/10.1088/0004-637X/765/2/104)
1572 Berg, D. A., Chisholm, J., Erb, D. K., et al. 2021, ApJ, 922, 170,
1573 doi: [10.3847/1538-4357/ac141b](https://doi.org/10.3847/1538-4357/ac141b)
1574 Berg, D. A., Erb, D. K., Auger, M. W., Pettini, M., & Brammer,
1575 G. B. 2018, ApJ, 859, 164, doi: [10.3847/1538-4357/aab7fa](https://doi.org/10.3847/1538-4357/aab7fa)
1576 Boquien, M., Burgarella, D., Roehlly, Y., et al. 2019, A&A, 622,
1577 A103, doi: [10.1051/0004-6361/201834156](https://doi.org/10.1051/0004-6361/201834156)
1578 Bouwens, R. J., Illingworth, G. D., Oesch, P. A., et al. 2011, ApJ,
1579 737, 90, doi: [10.1088/0004-637X/737/2/90](https://doi.org/10.1088/0004-637X/737/2/90)
1580 Boyett, K., Bunker, A. J., Curtis-Lake, E., et al. 2024, arXiv
1581 e-prints, arXiv:2401.16934, doi: [10.48550/arXiv.2401.16934](https://doi.org/10.48550/arXiv.2401.16934)
1582 Bruzual, G., & Charlot, S. 2003, MNRAS, 344, 1000,
1583 doi: [10.1046/j.1365-8711.2003.06897.x](https://doi.org/10.1046/j.1365-8711.2003.06897.x)
1584 Calzetti, D., Armus, L., Bohlin, R. C., et al. 2000, ApJ, 533, 682,
1585 doi: [10.1086/308692](https://doi.org/10.1086/308692)

1586 Cameron, A. J., Saxena, A., Bunker, A. J., et al. 2023, A&A, 677,
1587 A115, doi: [10.1051/0004-6361/202346107](https://doi.org/10.1051/0004-6361/202346107)
1588 Cardamone, C., Schawinski, K., Sarzi, M., et al. 2009, MNRAS,
1589 399, 1191, doi: [10.1111/j.1365-2966.2009.15383.x](https://doi.org/10.1111/j.1365-2966.2009.15383.x)
1590 Carnall, A. C., McLure, R. J., Dunlop, J. S., & Davé, R. 2018,
1591 MNRAS, 480, 4379, doi: [10.1093/mnras/sty2169](https://doi.org/10.1093/mnras/sty2169)
1592 Castellano, M., Belfiori, D., Pentericci, L., et al. 2023, A&A, 675,
1593 A121, doi: [10.1051/0004-6361/202346069](https://doi.org/10.1051/0004-6361/202346069)
1594 Chabrier, G. 2003, PASP, 115, 763, doi: [10.1086/376392](https://doi.org/10.1086/376392)
1595 Chen, Z., Stark, D. P., Mason, C., et al. 2024, MNRAS, 528, 7052,
1596 doi: [10.1093/mnras/stae455](https://doi.org/10.1093/mnras/stae455)
1597 Chevallard, J., Charlot, S., Senchyna, P., et al. 2018, MNRAS, 479,
1598 3264, doi: [10.1093/mnras/sty1461](https://doi.org/10.1093/mnras/sty1461)
1599 Chisholm, J., Saldana-Lopez, A., Flury, S., et al. 2022, MNRAS,
1600 517, 5104, doi: [10.1093/mnras/stac2874](https://doi.org/10.1093/mnras/stac2874)
1601 Choustikov, N., Katz, H., Saxena, A., et al. 2024, MNRAS, 529,
1602 3751, doi: [10.1093/mnras/stae776](https://doi.org/10.1093/mnras/stae776)

Table 8. Bagpipes parameters used in the SED fitting process. Note that Bagpipes assumes

Parameter	Range	Prior
Continuity Non-Parametric Star Formation History Model (Leja et al. 2019)		
Mass Formed in Each Time Bin ($\log_{10} M/M_{\odot}$)	[1,13]	Uniform
Stellar Metallicity (Z_{\odot})	5×10^{-4} , 2]	Uniform
Time Bin Edges (Myr)	0, 3, 10, 30, 100, 300, 1000, 3000, 6000	–
Stellar Population Synthesis Model (BPASS v2.2.1 Stanway & Eldridge 2018)		
Initial mass function – Broken Power Law (Upper Mass: $300 M_{\odot}$)	IMF	–
Nebular Emission Line Spectrum (Cloudy v17.03; recomputed for $n_e = 800 \text{ cm}^{-3}$)		
Ionisation parameter ($\log_{10} U$)	[−4, −1]	Uniform
Gas Metallicity (Z_{\odot})	0.065	Fixed
Dust Attenuation Model (Calzetti et al. 2000)		
V-band dust attenuation (A_V ; mag)	0.0	Fixed
$E(B - V)_{\text{nebular}}/E(B - V)_{\text{stellar}}$	1.0	Fixed
Slope delta of the power law modifying the attenuation curve	0.0	Fixed
Dust Emission Model (Draine et al. 2014)		
Mass fraction of PAH (q_{PAH})	2.50	Fixed
Minimum Radiation Field (U_{min})	1.0	Fixed
Fraction illuminated from U_{min} to U_{max} (γ)	0.1	Fixed

1603 Civano, F., Marchesi, S., Comastri, A., et al. 2016, ApJ, 819, 62,
 1604 doi: [10.3847/0004-637X/819/1/62](https://doi.org/10.3847/0004-637X/819/1/62)
 1605 Cohn, J. H., Leja, J., Tran, K.-V. H., et al. 2018, ApJ, 869, 141,
 1606 doi: [10.3847/1538-4357/aaed3d](https://doi.org/10.3847/1538-4357/aaed3d)
 1607 Davies, R. L., Förster Schreiber, N. M., Genzel, R., et al. 2021,
 1608 ApJ, 909, 78, doi: [10.3847/1538-4357/abd551](https://doi.org/10.3847/1538-4357/abd551)
 1609 Dawson, S., Rhoads, J. E., Malhotra, S., et al. 2007, ApJ, 671,
 1610 1227, doi: [10.1086/522908](https://doi.org/10.1086/522908)
 1611 De Barros, S., Oesch, P. A., Labbé, I., et al. 2019, MNRAS, 489,
 1612 2355, doi: [10.1093/mnras/stz940](https://doi.org/10.1093/mnras/stz940)
 1613 de Barros, S., Vanzella, E., Amorín, R., et al. 2016, A&A, 585,
 1614 A51, doi: [10.1051/0004-6361/201527046](https://doi.org/10.1051/0004-6361/201527046)
 1615 Ding, X., Silverman, J., Treu, T., et al. 2020, ApJ, 888, 37,
 1616 doi: [10.3847/1538-4357/ab5b90](https://doi.org/10.3847/1538-4357/ab5b90)
 1617 Draine, B. T., Aniano, G., Krause, O., et al. 2014, ApJ, 780, 172,
 1618 doi: [10.1088/0004-637X/780/2/172](https://doi.org/10.1088/0004-637X/780/2/172)
 1619 Emami, N., Siana, B., Alavi, A., et al. 2020, ApJ, 895, 116,
 1620 doi: [10.3847/1538-4357/ab8f97](https://doi.org/10.3847/1538-4357/ab8f97)
 1621 Endsley, R., Stark, D. P., Charlot, S., et al. 2021a, MNRAS, 502,
 1622 6044, doi: [10.1093/mnras/stab432](https://doi.org/10.1093/mnras/stab432)
 1623 Endsley, R., Stark, D. P., Chevallard, J., & Charlot, S. 2021b,
 1624 MNRAS, 500, 5229, doi: [10.1093/mnras/staa3370](https://doi.org/10.1093/mnras/staa3370)
 1625 Erb, D. K., Steidel, C. C., Shapley, A. E., et al. 2006, ApJ, 646,
 1626 107, doi: [10.1086/504891](https://doi.org/10.1086/504891)
 1627 Faisst, A. L. 2016, ApJ, 829, 99, doi: [10.3847/0004-637X/829/2/99](https://doi.org/10.3847/0004-637X/829/2/99)
 1628 Faisst, A. L., Capak, P., Hsieh, B. C., et al. 2016, ApJ, 821, 122,
 1629 doi: [10.3847/0004-637X/821/2/122](https://doi.org/10.3847/0004-637X/821/2/122)
 1630 Faucher-Giguère, C.-A. 2018, MNRAS, 473, 3717,
 1631 doi: [10.1093/mnras/stx2595](https://doi.org/10.1093/mnras/stx2595)

1632 Ferland, G. J., Korista, K. T., Verner, D. A., et al. 1998, PASP, 110,
 1633 761, doi: [10.1086/316190](https://doi.org/10.1086/316190)
 1634 Ferland, G. J., Porter, R. L., van Hoof, P. A. M., et al. 2013,
 1635 RMxAA, 49, 137, doi: [10.48550/arXiv.1302.4485](https://doi.org/10.48550/arXiv.1302.4485)
 1636 Ferland, G. J., Chatzikos, M., Guzmán, F., et al. 2017, RMxAA,
 1637 53, 385, doi: [10.48550/arXiv.1705.10877](https://doi.org/10.48550/arXiv.1705.10877)
 1638 Fernandes, R. C., Leão, J. R. S., & Lacerda, R. R. 2003, MNRAS,
 1639 340, 29, doi: [10.1046/j.1365-8711.2003.06203.x](https://doi.org/10.1046/j.1365-8711.2003.06203.x)
 1640 Feroz, F., & Hobson, M. P. 2008, MNRAS, 384, 449,
 1641 doi: [10.1111/j.1365-2966.2007.12353.x](https://doi.org/10.1111/j.1365-2966.2007.12353.x)
 1642 Feroz, F., Hobson, M. P., & Bridges, M. 2009, MNRAS, 398,
 1643 1601, doi: [10.1111/j.1365-2966.2009.14548.x](https://doi.org/10.1111/j.1365-2966.2009.14548.x)
 1644 Feroz, F., Hobson, M. P., Cameron, E., & Pettitt, A. N. 2019, The
 1645 Open Journal of Astrophysics, 2, 10,
 1646 doi: [10.21105/astro.1306.2144](https://doi.org/10.21105/astro.1306.2144)
 1647 Finkelstein, S. L., Bagley, M., Song, M., et al. 2022, ApJ, 928, 52,
 1648 doi: [10.3847/1538-4357/ac3aed](https://doi.org/10.3847/1538-4357/ac3aed)
 1649 Foreman-Mackey, D., Hogg, D. W., Lang, D., & Goodman, J.
 1650 2013, PASP, 125, 306, doi: [10.1086/670067](https://doi.org/10.1086/670067)
 1651 Forrest, B., Tran, K.-V. H., Broussard, A., et al. 2017, ApJL, 838,
 1652 L12, doi: [10.3847/2041-8213/aa653b](https://doi.org/10.3847/2041-8213/aa653b)
 1653 Genel, S., Vogelsberger, M., Springel, V., et al. 2014, MNRAS,
 1654 445, 175, doi: [10.1093/mnras/stu1654](https://doi.org/10.1093/mnras/stu1654)
 1655 Genzel, R., Förster Schreiber, N. M., Rosario, D., et al. 2014, ApJ,
 1656 796, 7, doi: [10.1088/0004-637X/796/1/7](https://doi.org/10.1088/0004-637X/796/1/7)
 1657 Goto, H., Shimasaku, K., Yamanaka, S., et al. 2021, ApJ, 923, 229,
 1658 doi: [10.3847/1538-4357/ac308b](https://doi.org/10.3847/1538-4357/ac308b)
 1659 Guo, H., Shen, Y., & Wang, S. 2018, PyQSOFit: Python code to fit
 1660 the spectrum of quasars, Astrophysics Source Code Library.
 1661 <http://ascl.net/1809.008>

- Guseva, N. G., Izotov, Y. I., & Thuan, T. X. 2000, *ApJ*, 531, 776, doi: [10.1086/308489](https://doi.org/10.1086/308489)
- Harris, C. R., Millman, K. J., van der Walt, S. J., et al. 2020, *Nature*, 585, 357, doi: [10.1038/s41586-020-2649-2](https://doi.org/10.1038/s41586-020-2649-2)
- Hasinger, G., Cappelluti, N., Brunner, H., et al. 2007, *ApJS*, 172, 29, doi: [10.1086/516576](https://doi.org/10.1086/516576)
- Ho, L. C., Filippenko, A. V., Sargent, W. L. W., & Peng, C. Y. 1997, *ApJS*, 112, 391, doi: [10.1086/313042](https://doi.org/10.1086/313042)
- Hoffman, M. D., Gelman, A., et al. 2014, *J. Mach. Learn. Res.*, 15, 1593
- Horne, K. 1986, *PASP*, 98, 609, doi: [10.1086/131801](https://doi.org/10.1086/131801)
- Inoue, A. K. 2011, *MNRAS*, 415, 2920, doi: [10.1111/j.1365-2966.2011.18906.x](https://doi.org/10.1111/j.1365-2966.2011.18906.x)
- Inoue, A. K., Shimizu, I., Iwata, I., & Tanaka, M. 2014, *MNRAS*, 442, 1805, doi: [10.1093/mnras/stu936](https://doi.org/10.1093/mnras/stu936)
- Ishigaki, M., Kawamata, R., Ouchi, M., et al. 2018, *ApJ*, 854, 73, doi: [10.3847/1538-4357/aaa544](https://doi.org/10.3847/1538-4357/aaa544)
- Isobe, Y., Ouchi, M., Nakajima, K., et al. 2023, *ApJ*, 956, 139, doi: [10.3847/1538-4357/acf376](https://doi.org/10.3847/1538-4357/acf376)
- Izotov, Y. I., Guseva, N. G., Fricke, K. J., Henkel, C., & Schaerer, D. 2017, *MNRAS*, 467, 4118, doi: [10.1093/mnras/stx347](https://doi.org/10.1093/mnras/stx347)
- Izotov, Y. I., Guseva, N. G., & Thuan, T. X. 2011, *ApJ*, 728, 161, doi: [10.1088/0004-637X/728/2/161](https://doi.org/10.1088/0004-637X/728/2/161)
- Izotov, Y. I., Schaerer, D., Thuan, T. X., et al. 2016, *MNRAS*, 461, 3683, doi: [10.1093/mnras/stw1205](https://doi.org/10.1093/mnras/stw1205)
- Izotov, Y. I., Stasińska, G., Meynet, G., Guseva, N. G., & Thuan, T. X. 2006, *A&A*, 448, 955, doi: [10.1051/0004-6361:20053763](https://doi.org/10.1051/0004-6361:20053763)
- Izotov, Y. I., Thuan, T. X., & Guseva, N. G. 2021a, *MNRAS*, 504, 3996, doi: [10.1093/mnras/stab1099](https://doi.org/10.1093/mnras/stab1099)
- Izotov, Y. I., Worseck, G., Schaerer, D., et al. 2021b, *MNRAS*, 503, 1734, doi: [10.1093/mnras/stab612](https://doi.org/10.1093/mnras/stab612)
- . 2018, *MNRAS*, 478, 4851, doi: [10.1093/mnras/sty1378](https://doi.org/10.1093/mnras/sty1378)
- Jeong, M.-S., Shapley, A. E., Sanders, R. L., et al. 2020, *ApJL*, 902, L16, doi: [10.3847/2041-8213/abba7a](https://doi.org/10.3847/2041-8213/abba7a)
- Jiang, T., Malhotra, S., Rhoads, J. E., & Yang, H. 2019, *ApJ*, 872, 145, doi: [10.3847/1538-4357/aace8a](https://doi.org/10.3847/1538-4357/aace8a)
- Juneau, S., Dickinson, M., Alexander, D. M., & Salim, S. 2011, *ApJ*, 736, 104, doi: [10.1088/0004-637X/736/2/104](https://doi.org/10.1088/0004-637X/736/2/104)
- Kaasinen, M., Bian, F., Groves, B., Kewley, L. J., & Gupta, A. 2017, *MNRAS*, 465, 3220, doi: [10.1093/mnras/stw2827](https://doi.org/10.1093/mnras/stw2827)
- Kennicutt, Robert C., J. 1998a, *ARA&A*, 36, 189, doi: [10.1146/annurev.astro.36.1.189](https://doi.org/10.1146/annurev.astro.36.1.189)
- . 1998b, *ApJ*, 498, 541, doi: [10.1086/305588](https://doi.org/10.1086/305588)
- Kewley, L. J., Nicholls, D. C., & Sutherland, R. S. 2019, *ARA&A*, 57, 511, doi: [10.1146/annurev-astro-081817-051832](https://doi.org/10.1146/annurev-astro-081817-051832)
- Khostovan, A. A., Malhotra, S., Rhoads, J. E., et al. 2024, *arXiv e-prints*, arXiv:2408.00080, doi: [10.48550/arXiv.2408.00080](https://doi.org/10.48550/arXiv.2408.00080)
- Khostovan, A. A., Sobral, D., Mobasher, B., et al. 2016, *MNRAS*, 463, 2363, doi: [10.1093/mnras/stw2174](https://doi.org/10.1093/mnras/stw2174)
- . 2018, *MNRAS*, 478, 2999, doi: [10.1093/mnras/sty925](https://doi.org/10.1093/mnras/sty925)
- Kim, K. J., Malhotra, S., Rhoads, J. E., & Yang, H. 2021, *ApJ*, 914, 2, doi: [10.3847/1538-4357/abf833](https://doi.org/10.3847/1538-4357/abf833)
- Konno, A., Ouchi, M., Shibuya, T., et al. 2018, *PASJ*, 70, S16, doi: [10.1093/pasj/psx131](https://doi.org/10.1093/pasj/psx131)
- Kriek, M., Shapley, A. E., Reddy, N. A., et al. 2015, *ApJS*, 218, 15, doi: [10.1088/0067-0049/218/2/15](https://doi.org/10.1088/0067-0049/218/2/15)
- Laigle, C., McCracken, H. J., Ilbert, O., et al. 2016, *ApJS*, 224, 24, doi: [10.3847/0067-0049/224/2/24](https://doi.org/10.3847/0067-0049/224/2/24)
- Lam, D., Bouwens, R. J., Labbé, I., et al. 2019, *A&A*, 627, A164, doi: [10.1051/0004-6361/201935227](https://doi.org/10.1051/0004-6361/201935227)
- Langeroodi, D., Hjorth, J., Chen, W., et al. 2023, *ApJ*, 957, 39, doi: [10.3847/1538-4357/acdbc1](https://doi.org/10.3847/1538-4357/acdbc1)
- Leitherer, C., & Heckman, T. M. 1995, *ApJS*, 96, 9, doi: [10.1086/192112](https://doi.org/10.1086/192112)
- Leja, J., Carnall, A. C., Johnson, B. D., Conroy, C., & Speagle, J. S. 2019, *ApJ*, 876, 3, doi: [10.3847/1538-4357/ab133c](https://doi.org/10.3847/1538-4357/ab133c)
- Leja, J., Johnson, B. D., Conroy, C., van Dokkum, P. G., & Byler, N. 2017, *ApJ*, 837, 170, doi: [10.3847/1538-4357/aa5ffe](https://doi.org/10.3847/1538-4357/aa5ffe)
- Levesque, E. M., & Leitherer, C. 2013, *ApJ*, 779, 170, doi: [10.1088/0004-637X/779/2/170](https://doi.org/10.1088/0004-637X/779/2/170)
- Levesque, E. M., & Richardson, M. L. A. 2014, *ApJ*, 780, 100, doi: [10.1088/0004-637X/780/1/100](https://doi.org/10.1088/0004-637X/780/1/100)
- Luridiana, V., Morisset, C., & Shaw, R. A. 2015, *A&A*, 573, A42, doi: [10.1051/0004-6361/201323152](https://doi.org/10.1051/0004-6361/201323152)
- Ly, C., Malkan, M. A., Rigby, J. R., & Nagao, T. 2016, *ApJ*, 828, 67, doi: [10.3847/0004-637X/828/2/67](https://doi.org/10.3847/0004-637X/828/2/67)
- Madau, P. 1995, *ApJ*, 441, 18, doi: [10.1086/175332](https://doi.org/10.1086/175332)
- Malhotra, S., & Rhoads, J. E. 2004, *ApJL*, 617, L5, doi: [10.1086/427182](https://doi.org/10.1086/427182)
- Marchesi, S., Civano, F., Elvis, M., et al. 2016, *ApJ*, 817, 34, doi: [10.3847/0004-637X/817/1/34](https://doi.org/10.3847/0004-637X/817/1/34)
- Marino, R. A., Rosales-Ortega, F. F., Sánchez, S. F., et al. 2013, *A&A*, 559, A114, doi: [10.1051/0004-6361/201321956](https://doi.org/10.1051/0004-6361/201321956)
- Mármol-Queraltó, E., McLure, R. J., Cullen, F., et al. 2016, *MNRAS*, 460, 3587, doi: [10.1093/mnras/stw1212](https://doi.org/10.1093/mnras/stw1212)
- Marques-Chaves, R., Álvarez-Márquez, J., Colina, L., et al. 2020, *MNRAS*, 499, L105, doi: [10.1093/mnras/lsaa160](https://doi.org/10.1093/mnras/lsaa160)
- Maseda, M. V., van der Wel, A., da Cunha, E., et al. 2013, *ApJL*, 778, L22, doi: [10.1088/2041-8205/778/1/L22](https://doi.org/10.1088/2041-8205/778/1/L22)
- Maseda, M. V., van der Wel, A., Rix, H.-W., et al. 2014, *ApJ*, 791, 17, doi: [10.1088/0004-637X/791/1/17](https://doi.org/10.1088/0004-637X/791/1/17)
- Masters, D., & Capak, P. 2011, *PASP*, 123, 638, doi: [10.1086/660023](https://doi.org/10.1086/660023)
- Matthee, J., Mackenzie, R., Simcoe, R. A., et al. 2023, *ApJ*, 950, 67, doi: [10.3847/1538-4357/acc846](https://doi.org/10.3847/1538-4357/acc846)
- Matthee, J., Sobral, D., Best, P., et al. 2017, *MNRAS*, 465, 3637, doi: [10.1093/mnras/stw2973](https://doi.org/10.1093/mnras/stw2973)
- Matthee, J. J. A., Sobral, D., Swinbank, A. M., et al. 2014, *MNRAS*, 440, 2375, doi: [10.1093/mnras/stu392](https://doi.org/10.1093/mnras/stu392)

- McLeod, D. J., McLure, R. J., & Dunlop, J. S. 2016, *MNRAS*, 459, 3812, doi: [10.1093/mnras/stw904](https://doi.org/10.1093/mnras/stw904)
- McLure, R. J., Dunlop, J. S., Bowler, R. A. A., et al. 2013, *MNRAS*, 432, 2696, doi: [10.1093/mnras/stt627](https://doi.org/10.1093/mnras/stt627)
- Naidu, R. P., Tacchella, S., Mason, C. A., et al. 2020, *ApJ*, 892, 109, doi: [10.3847/1538-4357/ab7cc9](https://doi.org/10.3847/1538-4357/ab7cc9)
- Nanayakkara, T., Brinchmann, J., Boogaard, L., et al. 2019, *A&A*, 624, A89, doi: [10.1051/0004-6361/201834565](https://doi.org/10.1051/0004-6361/201834565)
- Narayanan, D., Lower, S., Torrey, P., et al. 2024, *ApJ*, 961, 73, doi: [10.3847/1538-4357/ad0966](https://doi.org/10.3847/1538-4357/ad0966)
- Nelson, D., Pillepich, A., Genel, S., et al. 2015, *Astronomy and Computing*, 13, 12, doi: [10.1016/j.ascom.2015.09.003](https://doi.org/10.1016/j.ascom.2015.09.003)
- Nishigaki, M., Ouchi, M., Nakajima, K., et al. 2023, *ApJ*, 952, 11, doi: [10.3847/1538-4357/accf14](https://doi.org/10.3847/1538-4357/accf14)
- Oesch, P. A., Bouwens, R. J., Illingworth, G. D., et al. 2014, *ApJ*, 786, 108, doi: [10.1088/0004-637X/786/2/108](https://doi.org/10.1088/0004-637X/786/2/108)
- Onodera, M., Shimakawa, R., Suzuki, T. L., et al. 2020, *ApJ*, 904, 180, doi: [10.3847/1538-4357/abc174](https://doi.org/10.3847/1538-4357/abc174)
- Ormerod, K., Conselice, C. J., Adams, N. J., et al. 2024, *MNRAS*, 527, 6110, doi: [10.1093/mnras/stad3597](https://doi.org/10.1093/mnras/stad3597)
- Paalvast, M., Verhamme, A., Straka, L. A., et al. 2018, *A&A*, 618, A40, doi: [10.1051/0004-6361/201832866](https://doi.org/10.1051/0004-6361/201832866)
- Papovich, C., Cole, J. W., Yang, G., et al. 2023, *ApJL*, 949, L18, doi: [10.3847/2041-8213/acc948](https://doi.org/10.3847/2041-8213/acc948)
- Pasha, I., & Miller, T. B. 2023, *Journal of Open Source Software*, 8, 5703, doi: [10.21105/joss.05703](https://doi.org/10.21105/joss.05703)
- Pei, Y. C. 1992, *ApJ*, 395, 130, doi: [10.1086/171637](https://doi.org/10.1086/171637)
- Pettini, M., & Pagel, B. E. J. 2004, *MNRAS*, 348, L59, doi: [10.1111/j.1365-2966.2004.07591.x](https://doi.org/10.1111/j.1365-2966.2004.07591.x)
- Pharo, J., Guo, Y., Koo, D. C., Forbes, J. C., & Guhathakurta, P. 2023, *ApJL*, 946, L5, doi: [10.3847/2041-8213/acb34d](https://doi.org/10.3847/2041-8213/acb34d)
- Prochaska, J., Hennawi, J., Westfall, K., et al. 2020a, *The Journal of Open Source Software*, 5, 2308, doi: [10.21105/joss.02308](https://doi.org/10.21105/joss.02308)
- Prochaska, J. X., Hennawi, J., Cooke, R., et al. 2020b, *pypeit/PypeIt: Release 1.0.0, v1.0.0*, Zenodo, Zenodo, doi: [10.5281/zenodo.3743493](https://doi.org/10.5281/zenodo.3743493)
- Pucha, R., Reddy, N. A., Dey, A., et al. 2022, *AJ*, 164, 159, doi: [10.3847/1538-3881/ac83a9](https://doi.org/10.3847/1538-3881/ac83a9)
- Rasappu, N., Smit, R., Labbé, I., et al. 2016, *MNRAS*, 461, 3886, doi: [10.1093/mnras/stw1484](https://doi.org/10.1093/mnras/stw1484)
- Reddy, N. A., Topping, M. W., Sanders, R. L., Shapley, A. E., & Brammer, G. 2023, *ApJ*, 952, 167, doi: [10.3847/1538-4357/acd754](https://doi.org/10.3847/1538-4357/acd754)
- Reddy, N. A., Topping, M. W., Shapley, A. E., et al. 2022, *ApJ*, 926, 31, doi: [10.3847/1538-4357/ac3b4c](https://doi.org/10.3847/1538-4357/ac3b4c)
- Rhoads, J. E., Malhotra, S., Dey, A., et al. 2000, *ApJL*, 545, L85, doi: [10.1086/317874](https://doi.org/10.1086/317874)
- Rinaldi, P., Caputi, K. I., Costantin, L., et al. 2023, *ApJ*, 952, 143, doi: [10.3847/1538-4357/acdc27](https://doi.org/10.3847/1538-4357/acdc27)
- Robertson, B. E., Furlanetto, S. R., Schneider, E., et al. 2013, *ApJ*, 768, 71, doi: [10.1088/0004-637X/768/1/71](https://doi.org/10.1088/0004-637X/768/1/71)
- Sanders, R. L., Shapley, A. E., Topping, M. W., Reddy, N. A., & Brammer, G. B. 2023, *ApJ*, 955, 54, doi: [10.3847/1538-4357/acedad](https://doi.org/10.3847/1538-4357/acedad)
- Sanders, R. L., Shapley, A. E., Kriek, M., et al. 2016, *ApJ*, 816, 23, doi: [10.3847/0004-637X/816/1/23](https://doi.org/10.3847/0004-637X/816/1/23)
- Sanders, R. L., Shapley, A. E., Jones, T., et al. 2021, *ApJ*, 914, 19, doi: [10.3847/1538-4357/abf4c1](https://doi.org/10.3847/1538-4357/abf4c1)
- Santos, S., Sobral, D., & Matthee, J. 2016, *MNRAS*, 463, 1678, doi: [10.1093/mnras/stw2076](https://doi.org/10.1093/mnras/stw2076)
- Saxena, A., Pentericci, L., Mirabelli, M., et al. 2020, *A&A*, 636, A47, doi: [10.1051/0004-6361/201937170](https://doi.org/10.1051/0004-6361/201937170)
- Schaerer, D. 2003, *A&A*, 397, 527, doi: [10.1051/0004-6361:20021525](https://doi.org/10.1051/0004-6361:20021525)
- Schaerer, D., Izotov, Y. I., Verhamme, A., et al. 2016, *A&A*, 591, L8, doi: [10.1051/0004-6361/201628943](https://doi.org/10.1051/0004-6361/201628943)
- Scoville, N., Aussel, H., Brusa, M., et al. 2007, *ApJS*, 172, 1, doi: [10.1086/516585](https://doi.org/10.1086/516585)
- Senchyna, P., Stark, D. P., Chevallard, J., et al. 2019, *MNRAS*, 488, 3492, doi: [10.1093/mnras/stz1907](https://doi.org/10.1093/mnras/stz1907)
- Shen, Y., Hall, P. B., Horne, K., et al. 2019, *ApJS*, 241, 34, doi: [10.3847/1538-4365/ab074f](https://doi.org/10.3847/1538-4365/ab074f)
- Shim, H., Chary, R.-R., Dickinson, M., et al. 2011, *ApJ*, 738, 69, doi: [10.1088/0004-637X/738/1/69](https://doi.org/10.1088/0004-637X/738/1/69)
- Shivaei, I., Reddy, N. A., Siana, B., et al. 2018, *ApJ*, 855, 42, doi: [10.3847/1538-4357/aaad62](https://doi.org/10.3847/1538-4357/aaad62)
- Silverman, J. D., Daddi, E., Rujopakarn, W., et al. 2018, *ApJ*, 868, 75, doi: [10.3847/1538-4357/aae64b](https://doi.org/10.3847/1538-4357/aae64b)
- Smit, R., Bouwens, R. J., Labbé, I., et al. 2014, *ApJ*, 784, 58, doi: [10.1088/0004-637X/784/1/58](https://doi.org/10.1088/0004-637X/784/1/58)
- Smit, R., Bouwens, R. J., Franx, M., et al. 2015, *ApJ*, 801, 122, doi: [10.1088/0004-637X/801/2/122](https://doi.org/10.1088/0004-637X/801/2/122)
- Sobral, D., Santos, S., Matthee, J., et al. 2018, *MNRAS*, 476, 4725, doi: [10.1093/mnras/sty378](https://doi.org/10.1093/mnras/sty378)
- Sparre, M., Hayward, C. C., Feldmann, R., et al. 2017, *MNRAS*, 466, 88, doi: [10.1093/mnras/stw3011](https://doi.org/10.1093/mnras/stw3011)
- Speagle, J. S., Steinhardt, C. L., Capak, P. L., & Silverman, J. D. 2014, *ApJS*, 214, 15, doi: [10.1088/0067-0049/214/2/15](https://doi.org/10.1088/0067-0049/214/2/15)
- Stanway, E. R., & Eldridge, J. J. 2018, *MNRAS*, 479, 75, doi: [10.1093/mnras/sty1353](https://doi.org/10.1093/mnras/sty1353)
- Stark, D. P., Ellis, R. S., Charlot, S., et al. 2017, *MNRAS*, 464, 469, doi: [10.1093/mnras/stw2233](https://doi.org/10.1093/mnras/stw2233)
- Stirpe, G. M. 1990, *A&AS*, 85, 1049
- Strom, A. L., Steidel, C. C., Rudie, G. C., et al. 2017, *ApJ*, 836, 164, doi: [10.3847/1538-4357/836/2/164](https://doi.org/10.3847/1538-4357/836/2/164)
- Sun, F., Egami, E., Pirzkal, N., et al. 2023, *ApJ*, 953, 53, doi: [10.3847/1538-4357/acd53c](https://doi.org/10.3847/1538-4357/acd53c)
- Swinbank, A. M., Harrison, C. M., Tiley, A. L., et al. 2019, *MNRAS*, 487, 381, doi: [10.1093/mnras/stz1275](https://doi.org/10.1093/mnras/stz1275)

- 1860 Tacchella, S., Conroy, C., Faber, S. M., et al. 2022, *ApJ*, 926, 134,
1861 doi: [10.3847/1538-4357/ac449b](https://doi.org/10.3847/1538-4357/ac449b)
- 1862 Tang, M., Stark, D. P., Chevallard, J., & Charlot, S. 2019, *MNRAS*,
1863 489, 2572, doi: [10.1093/mnras/stz2236](https://doi.org/10.1093/mnras/stz2236)
- 1864 Tang, M., Stark, D. P., & Ellis, R. S. 2022, *MNRAS*, 513, 5211,
1865 doi: [10.1093/mnras/stac1280](https://doi.org/10.1093/mnras/stac1280)
- 1866 Tang, M., Stark, D. P., Chen, Z., et al. 2023, *MNRAS*, 526, 1657,
1867 doi: [10.1093/mnras/stad2763](https://doi.org/10.1093/mnras/stad2763)
- 1868 Taylor, A. J., Barger, A. J., Cowie, L. L., Hu, E. M., & Songaila, A.
1869 2020, *ApJ*, 895, 132, doi: [10.3847/1538-4357/ab8ada](https://doi.org/10.3847/1538-4357/ab8ada)
- 1870 Thomas, D., Steele, O., Maraston, C., et al. 2013, *MNRAS*, 431,
1871 1383, doi: [10.1093/mnras/stt261](https://doi.org/10.1093/mnras/stt261)
- 1872 Torralba-Torregrosa, A., Renard, P., Spinoso, D., et al. 2024, *arXiv*
1873 e-prints, *arXiv:2407.19020*, doi: [10.48550/arXiv.2407.19020](https://doi.org/10.48550/arXiv.2407.19020)
- 1874 van der Wel, A., Straughn, A. N., Rix, H. W., et al. 2011, *ApJ*, 742,
1875 111, doi: [10.1088/0004-637X/742/2/111](https://doi.org/10.1088/0004-637X/742/2/111)
- 1876 Vanzella, E., Caminha, G. B., Calura, F., et al. 2020, *MNRAS*, 491,
1877 1093, doi: [10.1093/mnras/stz2286](https://doi.org/10.1093/mnras/stz2286)
- 1878 Vogelsberger, M., Genel, S., Springel, V., et al. 2014a, *Nature*, 509,
1879 177, doi: [10.1038/nature13316](https://doi.org/10.1038/nature13316)
- 1880 —. 2014b, *MNRAS*, 444, 1518, doi: [10.1093/mnras/stu1536](https://doi.org/10.1093/mnras/stu1536)
- 1881 Weaver, J. R., Kauffmann, O. B., Ilbert, O., et al. 2022, *ApJS*, 258,
1882 11, doi: [10.3847/1538-4365/ac3078](https://doi.org/10.3847/1538-4365/ac3078)
- 1883 Whitler, L., Stark, D. P., Endsley, R., et al. 2024, *MNRAS*, 529,
1884 855, doi: [10.1093/mnras/stae516](https://doi.org/10.1093/mnras/stae516)
- 1885 Wold, I. G. B., Malhotra, S., Rhoads, J., et al. 2022, *ApJ*, 927, 36,
1886 doi: [10.3847/1538-4357/ac4997](https://doi.org/10.3847/1538-4357/ac4997)
- 1887 Yang, G., Boquien, M., Brandt, W. N., et al. 2022a, *ApJ*, 927, 192,
1888 doi: [10.3847/1538-4357/ac4971](https://doi.org/10.3847/1538-4357/ac4971)
- 1889 Yang, H., Malhotra, S., Gronke, M., et al. 2016, *ApJ*, 820, 130,
1890 doi: [10.3847/0004-637X/820/2/130](https://doi.org/10.3847/0004-637X/820/2/130)
- 1891 Yang, H., Malhotra, S., Rhoads, J. E., et al. 2017a, *ApJ*, 838, 4,
1892 doi: [10.3847/1538-4357/aa6337](https://doi.org/10.3847/1538-4357/aa6337)
- 1893 Yang, H., Malhotra, S., Rhoads, J. E., & Wang, J. 2017b, *ApJ*, 847,
1894 38, doi: [10.3847/1538-4357/aa8809](https://doi.org/10.3847/1538-4357/aa8809)
- 1895 Yang, H., Malhotra, S., Gronke, M., et al. 2017c, *ApJ*, 844, 171,
1896 doi: [10.3847/1538-4357/aa7d4d](https://doi.org/10.3847/1538-4357/aa7d4d)
- 1897 Yang, L., Morishita, T., Leethochawalit, N., et al. 2022b, *ApJL*,
1898 938, L17, doi: [10.3847/2041-8213/ac8803](https://doi.org/10.3847/2041-8213/ac8803)
- 1899 Zolotov, A., Dekel, A., Mandelker, N., et al. 2015, *MNRAS*, 450,
1900 2327, doi: [10.1093/mnras/stv740](https://doi.org/10.1093/mnras/stv740)